



HD 207897 b: A dense sub-Neptune transiting a nearby and bright K-type star

N. Heidari, I. Boisse, J. Orell-Miquel, G. Hébrard, L. Acuña, N. C. Hara, J. Lillo-Box, J. D. Eastman, L. Arnold, N. Astudillo-Defru, et al.

► To cite this version:

N. Heidari, I. Boisse, J. Orell-Miquel, G. Hébrard, L. Acuña, et al.. HD 207897 b: A dense sub-Neptune transiting a nearby and bright K-type star. *Astronomy and Astrophysics - A&A*, 2022, 658, pp.A176. 10.1051/0004-6361/202141429 . hal-03580996

HAL Id: hal-03580996

<https://hal.science/hal-03580996>

Submitted on 18 Feb 2022

HAL is a multi-disciplinary open access archive for the deposit and dissemination of scientific research documents, whether they are published or not. The documents may come from teaching and research institutions in France or abroad, or from public or private research centers.

L'archive ouverte pluridisciplinaire **HAL**, est destinée au dépôt et à la diffusion de documents scientifiques de niveau recherche, publiés ou non, émanant des établissements d'enseignement et de recherche français ou étrangers, des laboratoires publics ou privés.

HD 207897 b: A dense sub-Neptune transiting a nearby and bright K-type star

N. Heidari^{1,2,3,*}, I. Boisse^{3,*}, J. Orell-Miquel^{4,5}, G. Hébrard^{6,7}, L. Acuña³, N. C. Hara⁸, J. Lillo-Box⁹, J. D. Eastman¹⁰, L. Arnold^{6,11}, N. Astudillo-Defru¹², V. Adibekyan^{13,14}, A. Bieryla¹⁰, X. Bonfils¹⁵, F. Bouchy⁸, T. Barclay^{17,16}, C. E. Brasseur¹⁸, S. Borgniet⁴⁰, V. Bourrier⁸, L. Buchhave⁴⁴, A. Behmard^{19,**}, C. Beard²⁰, N. M. Batalha²¹, B. Courcol⁸, P. Cortés-Zuleta³, K. Collins¹⁰, A. Carmona¹⁵, I. J. M. Crossfield²², A. Chontos^{23,**}, X. Delfosse¹⁵, S. Dalal⁷, M. Deleuil³, O. D. S. Demangeon^{13,14}, R. F. Díaz²⁴, X. Dumusque⁸, T. Daylan^{25,***}, D. Dragomir²⁶, E. Delgado Mena¹³, C. Dressing²⁷, F. Dai²⁸, P. A. Dalba^{29,****}, D. Ehrenreich⁸, T. Forveille¹⁵, B. Fulton³⁰, T. Fetherolf²⁹, G. Gaisné¹⁵, S. Giacalone²⁷, N. Riazi¹, S. Hoyer³, M. J. Hobson^{31,32}, A. W. Howard³³, D. Huber²³, M. L. Hill²⁹, L. A. Hirsch³⁴, H. Isaacson^{27,35}, J. Jenkins⁴⁶, S. R. Kane²⁹, F. Kiefer^{7,40}, R. Luque^{4,5}, D. W. Latham¹⁰, J. Lubin²⁰, T. Lopez³, O. Mousis³, C. Moutou⁴¹, G. Montagnier⁶, L. Mignon¹⁵, A. Mayo²⁷, T. Močnik³⁹, J. M. A. Murphy^{21,**}, E. Palte^{4,5}, F. Pepe⁸, E. A. Petigura³⁶, J. Rey³⁷, G. Ricker²⁵, P. Robertson²⁰, A. Roy^{18,38}, R. A. Rubenzahl^{33,**}, L. J. Rosenthal³³, A. Santerne³, N. C. Santos^{13,14}, S. G. Sousa¹³, K. G. Stassun⁴², M. Stalport⁸, N. Scarsdale²¹, P. A. Strøm^{7,47,48}, S. Seager^{25,49,50}, D. Segransan⁸, P. Tenenbaum⁴³, R. Trongsgaard⁴⁴, S. Udry⁸, R. Vanderspek²⁵, F. Vakili², J. Winn⁴⁵, and L. M. Weiss²³

(Affiliations can be found after the references)

Received 29 May 2021 / Accepted 8 September 2021

ABSTRACT

We present the discovery and characterization of a transiting sub-Neptune that orbits the nearby (28 pc) and bright ($V = 8.37$) K0V star HD 207897 (TOI-1611) with a 16.20-day period. This discovery is based on photometric measurements from the Transiting Exoplanet Survey Satellite mission and radial velocity (RV) observations from the SOPHIE, Automated Planet Finder, and HIRES high-precision spectrographs. We used EXOFASTv2 to model the parameters of the planet and its host star simultaneously, combining photometric and RV data to determine the planetary system parameters. We show that the planet has a radius of $2.50 \pm 0.08 R_E$ and a mass of either $14.4 \pm 1.6 M_E$ or $15.9 \pm 1.6 M_E$ with nearly equal probability. The two solutions correspond to two possibilities for the stellar activity period. The density accordingly is either $5.1 \pm 0.7 \text{ g cm}^{-3}$ or $5.5^{+0.8}_{-0.7} \text{ g cm}^{-3}$, making it one of the relatively rare dense sub-Neptunes. The existence of this dense planet at only 0.12 AU from its host star is unusual in the currently observed sub-Neptune ($2 < R_E < 4$) population. The most likely scenario is that this planet has migrated to its current position.

Key words. planets and satellites: detection – stars: activity – planets and satellites: individual: HD 207897 – planets and satellites: individual: TOI-1611 – planets and satellites: individual: TIC ID 264678534

1. Introduction

The brightness of more than 200 000 stars has been monitored by Transiting Exoplanet Survey Satellite (TESS) (Ricker et al. 2015) with two-minute cadence during its two-year primary mission. The observed stars are closer and brighter (typically 30–100 times brighter) than the stars *Kepler* surveyed. This offers us a unique opportunity for furthering our knowledge in planetary science with follow-up observations: those from ground-based high-precision spectrographs to confirm the planetary nature and mass measurement, which together with the radius allows us to determine the bulk composition of planets; and ground- and space-based observations to provide atmospheric characterization, for instance, with the upcoming *James Webb* Space Telescope (Gardner et al. 2006).

The NASA *Kepler* mission (Borucki et al. 2010) has discovered a large number of planets of intermediate size, with radii

between those of Earth and Neptune. They are also known as sub-Neptunes. Because the size of planets is directly dependent on the physical mechanisms in their formation and evolution, the absence of sub-Neptunes in our Solar System and their abundance among the exoplanet population has raised numerous fundamental questions. Many theoretical and statistical studies have been made of such planets. Rogers (2015) showed that most planets with $R > 1.6 R_E$ have a low density and are inconsistent with a purely rocky composition. Fulton et al. (2017) demonstrated that the sub-Neptunes' distribution of radii is bimodal, with two peaks centered at $1.2 R_E$ and $2.4 R_E$. This reveals a gap in planet radii between $1.5\text{--}2.0 R_E$. While this bimodal distribution can be explained by photoevaporation (Owen & Wu 2013, 2017; Lopez & Fortney 2014) and core-powered mass loss (Ginzburg et al. 2016, 2018), the composition and origin of close-in sub-Neptunes are not yet clear. Additional detections and precise characterizations are the keys to progress in answering our questions about their nature. One of the primary goals of TESS is to measure the mass of at least 50 transiting planets with a radius smaller than 4 Earth radii (Ricker et al. 2015). As of 22 April 2021, TESS has found more than

* Corresponding authors; N. Heidari (email: neda.heidari@lam.fr), I. Boisse (email: isabelle.boisse@lam.fr).

** NSF Graduate Research Fellow.

*** Kavli Fellow.

**** NSF Astronomy and Astrophysics Postdoctoral Fellow.

750 candidates¹ (so-called TESS objects of interest, or TOI) with radii smaller than $4 R_E$. To date, 122 of them have been confirmed and have a mass measurement (e.g., Dragomir et al. 2019; Günther et al. 2019; Nielsen et al. 2020).

Here, we announce the detection and characterization of a sub-Neptune orbiting a bright ($V = 8.4$) K0 star using TESS photometric data and SOPHIE, Automated Planet Finder (APF), and HIRES RVs. In Sect. 2 we describe the variety of observations that were used to characterize the HD 207897 (TOI-1611) system, including photometric, spectroscopic, and high-resolution imaging data. In Sect. 3 we analyze the data and present the characterization of the host star and planet, combining models on RVs and transit data. Finally, we present our discussion and conclude in Sect. 4.

2. Observations

In this section, we provide a summary of all observations of HD 207897 taken by TESS and ground-based facilities.

2.1. TESS photometry

TESS planned to observe 80% of the sky in 26 sectors for 2 yr. Each sector lasts for approximately 27 days, and the sectors partially overlap². Because HD 207897 is located near the north ecliptic pole where sectors overlap, it appears in many sectors. As reported in the Web TESS Viewing Tool (WTV)³, HD 207897 observations were taken in five sectors divided into two continuous periods from sectors 18–20 and 25–26, with a total time span of 131 days. After observations of sector 18 were completed, the MIT Quick Look pipeline (QLP; Huang et al. 2020a,b) detected the signature of two transits of HD 207897 b at a period of 16.20 d, and an alert was issued on 19 December 2019 by the TESS Science Office. No transits occurred during sector 19 as the sole transit fell in the data gap between the two orbits. After observations of sector 20 were downlinked, the Science Processing Operations Center (SPOC; Jenkins et al. 2016) at NASA Ames Research Center conducted a transit search (Jenkins 2002; Jenkins et al. 2010) and detected two transits of HD 207897 b at a signal-to-noise ratio (S/N) of 23.3. A limb-darkened transit model was fitted to the transit signature (Li et al. 2019), which passed all the diagnostic tests presented in the Data Validation report (Twicken et al. 2018), including the odd-even transit depth test, the ghost diagnostic test, and the difference-image centroiding test, which located the source of the transit signatures within 0.42 ± 2.5 arcsec of the target star HD 207897. Two additional transits were observed and detected in sector 25, and one more transit occurred in sector 26. A multisector search of sectors 18–26 by the SPOC detected 7 transit events of HD 207897 b in total at an S/N of 34.3 and an average depth of 913.7 ± 21.1 ppm. No additional transiting-planet signatures were detected in any of the SPOC or QLP runs.

We used the short-cadence (2 min) observations of TESS data from these five sectors in our photometric analysis, which we present in Sect. 3.2. These data were reduced by the SPOC Pipeline and are publicly available on Mikulski Archive for Space Telescopes (MAST)⁴.

¹ <https://tess.mit.edu/publications/>

² <https://tess.mit.edu/observations>

³ <https://heasarc.gsfc.nasa.gov/cgi-bin/tess/webtess/wtv.py>

⁴ <https://mast.stsci.edu/portal/Mashup/Clients/Mast/Portal.html>

2.2. High-resolution spectroscopy

2.2.1. SOPHIE

Before TESS observations, HD 207897 had been monitored by the SOPHIE spectrograph (Perruchot et al. 2008; Bouchy et al. 2013) between 2012 and 2015. The star measurements were conducted as a part of the Recherche de Planètes Extrasolaires (RPE) subprogram dedicated to detecting Neptunes and Super-Earths orbiting nearby and bright solar-type stars (Bouchy et al. 2009; Courcol et al. 2015; Hara et al. 2020). The observations were performed using high-resolution mode (resolution power of $\lambda/\Delta\lambda \approx 75\,000$) with a simultaneous thorium-argon (Th-Ar) calibration lamp, allowing us to monitor the instrumental drift. We collected 44 high-resolution spectra with an RV root mean square (RMS) of 6.9 m s^{-1} (see Sect. 3.3.1 for more details about the derivation of the RVs). A first analysis of the data in 2015 showed a periodicity close to 16.3 d. However, our preliminary analysis based on an erroneous estimate of the rotational period of the star caused us to attribute the 16.3 d signal to stellar spot modulation at $P_{\text{rot}}/2$, and observations of the star were stopped. After the release of the TESS data, we resumed SOPHIE observations to gather more data to better separate the activity signal and planetary RV variation, and also to search for other possible planets. The star was observed again in 2020 with a simultaneous Fabry-Perot (FP) reference spectrum. Twenty-four additional high-resolution spectra with an RV RMS of 4.43 m s^{-1} were gathered.

Our final SOPHIE dataset includes 68 spectra. With an exposure time ranging from 1000 to 1500 s, we achieved a median S/N of 97.7 per pixel at 550 nm. The mean RV uncertainty, computed using the quadratic sum of photon noise and wavelength calibration error, is 1.7 m s^{-1} . The RV data set are presented in Table A.1 after the corrections described in Sect. 3.3.1 were applied.

2.2.2. HIRES

From the summit of Maunakea, we first observed HD 207897 using the Keck I telescope and HIRES spectrometer (Vogt 1994) from 2003 July 7 as part of the California Planet Search, and additional RVs were collected for 11 months beginning on 2020 January 21. Thirty-seven RVs were collected using the B5 decker ($0.87'' \times 5.0''$), resulting in a resolution of 50 000. The median exposure time was 231 s, the average S/N per pixel was 220, and the internal uncertainty was 1.04 m s^{-1} . The Doppler pipeline and observing setup follows the California Planet Search procedure outlined in Howard et al. (2010). The RV data set are presented in Table A.2. We note that data before 2004 July 9 (three data points) used a different CCD detector. For the sake of simplicity, we only used them in our RV periodogram by applying an offset term (Fig. 1).

2.2.3. APF

From the summit of Mt. Hamilton at the Lick Observatory, we collected 23 RVs of HD 207897 using the Levy Spectrograph (Burt et al. 2014) on the APF from 2020 June 2 until 2021 February 28. Twenty-three RVs were collected. Their median exposure time was 1200s, the S/N per pixel was 86, and the internal uncertainty was 3.0 m s^{-1} . With a resolution of 100 000, this slit-fed spectrograph uses the iodine-cell technique to calculate RVs according to Butler et al. (1996). For additional details on the instrumental setup and data reduction, see Fulton et al. (2015). The full list of corrected RVs can be found in Table A.3.

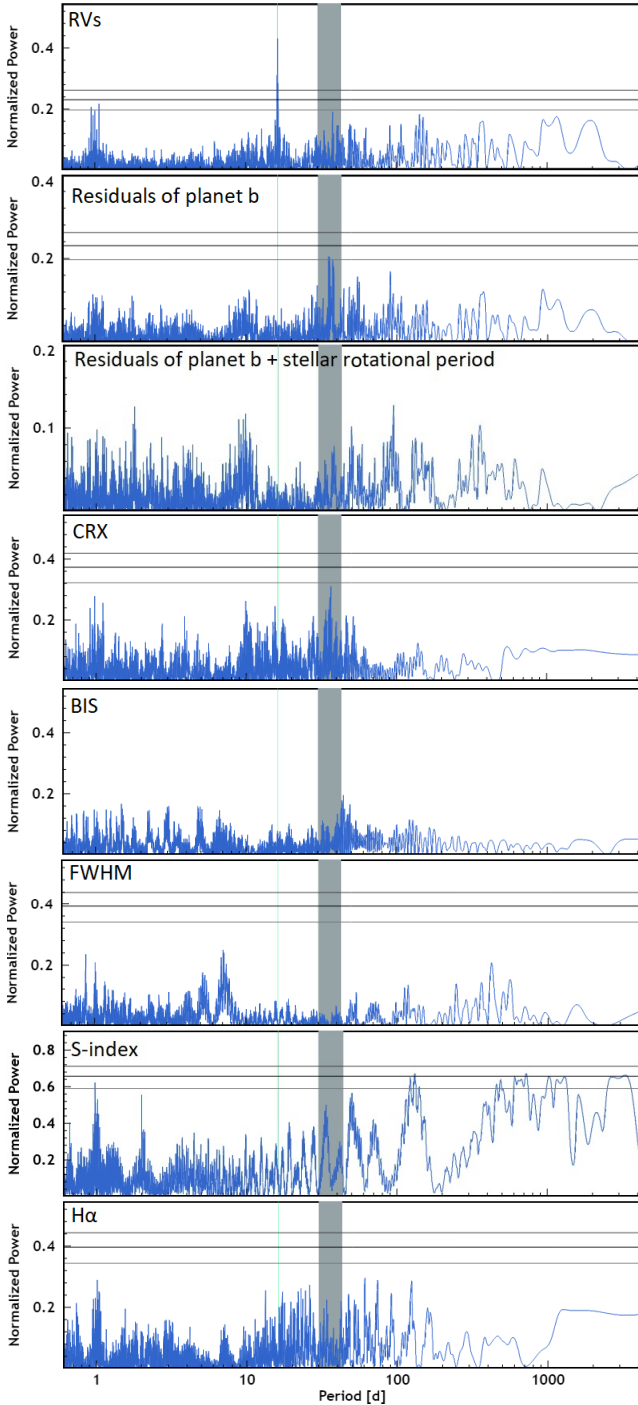


Fig. 1. Normalized periodograms of RVs and activity indexes for HD 207897. *From top to bottom:* RVs, residual of RVs after a Keplerian fit on 16.20 d, residuals of the fit on the planet and stellar rotation signal, CRX, bisector, FWHM, and $H\alpha$ index. The vertical cyan line marks the position of the highest peak in the RV periodogram at 16.20 d and shows no corresponding peak in the stellar activity periodograms. Horizontal lines indicate the 0.1, 1, and 10% FAP level from top to bottom. The vertical gray strip highlights the position of the rotational stellar period as estimated in Sect. 3.3.2.

2.2.4. FIES

From the Roque de los Muchachos Observatory in La Palma, Spain, we observed with the Fibre-fed Échelle Spectrograph (FIES; [Telting et al. 2014](#)) at the 2.56 m Nordic Optical Telescope and obtained four spectra between 2019 December 27 and

2020 January 15. We used the high-resolution fibre ($R \sim 67\,000$) and extracted the spectra following [Buchhave et al. \(2010\)](#). The S/N per resolution element at 550 nm ranges between 62 and 127. We used the FIES data for stellar classification (see Sect. 3.1) and refrained from including them in the RV analysis because all the observations were acquired near phases 0.25 and 0.75.

2.2.5. TRES

From the Fred Lawrence Whipple Observatory (FLWO) at the top of Mt. Hopkins, Arizona, USA, we observed with the 1.5 m Tillinghast Reflector Telescope using the Tillinghast Reflector Echelle Spectrograph (TRES; [Fűrész 2008](#); [Mink 2011](#)) to obtain one spectrum ($S/N \sim 36$) on UT 31 December 2019. TRES is a fiber-fed optical spectrograph with a resolving power of $R \sim 44\,000$. The spectrum was extracted following the procedures outlined in [Buchhave et al. \(2010\)](#) and was used to derive stellar parameters as described in Sect. 3.1.

2.3. High spatial resolution imaging

We used the AstraLux high spatial resolution camera ([Hormuth et al. 2008](#)) at the 2.2 m telescope of the Calar Alto Observatory (CAHA, Almeria, Spain) to unveil possible close companions to HD 207897. This instrument applies the lucky-imaging technique to retrieve diffraction-limited images from point source objects by acquiring thousands of short-exposure frames that freeze atmospheric variations and thus produce diffraction-limited images. We observed this target on 2020 February 26 under good weather conditions and a mean seeing of 0.9 arcsec. The brightness of this target allowed us to obtain 11 000 frames with an individual exposure time of 10 milliseconds. We used the Sloan Digital Sky Survey z filter (SDSSz), which is best suited for obtaining the highest possible resolution with AstraLux. We also used a field of view windowed to 6×6 arcsec. All frames were reduced by the instrument pipeline ([Hormuth et al. 2008](#)), which performs the basic reduction (bias subtraction and flat field correction), aligns all frames, and measures the Strehl ratio ([Strehl 1902](#)) of the individual images. This metric was then used to select the best images to perform the final stacking. We used the best 10% of the frames to produce the final high-resolution image. The final image does not show signs of close companions. We performed a dedicated search by removing the instrumental point spread function scaled to the target peak flux. No additional sources were present in the image. We then followed the procedures described in [Lillo-Box et al. \(2012, 2014\)](#) by using our own developed astrasens package⁵ to obtain the sensitivity of our image by performing an injection or retrieval of artificial sources. The sensitivity curve is shown in Fig. 2.

By using this sensitivity curve, we additionally estimated the probability of an undetected blended source in our high-spatial resolution image (BSC, see the procedure described in [Lillo-Box et al. 2014](#)). We use a python implementation of this approach (bsc, by J. Lillo-Box), which uses the TRILEGAL⁶ galactic model (v1.6 [Girardi et al. 2012](#)) to retrieve a simulated source population of the region around the corresponding target⁷. This simulated population is used to compute the density of stars around the target position (radius $r = 1''$) and to derive the probability of chance alignment at a given contrast

⁵ <https://github.com/jlillo/astrasens>

⁶ <http://stev.oapd.inaf.it/cgi-bin/trilegal>

⁷ This is done in python by using the [Bhatti et al. \(2020\)](#) implementation by [Bhatti et al. \(2020\)](#).

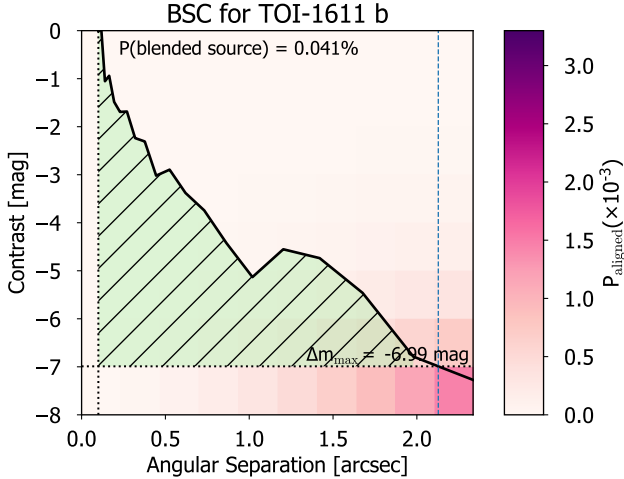


Fig. 2. Blended source confidence curve from the AstraLux SDSSz image (solid black line). The color in each angular separation and contrast bin represents the probability of a chance-aligned source with these properties at the location of the target, based on the TRILEGAL model (see Sect. 2.3). The maximum contrast of a blended binary capable of mimicking the planet transit depth is shown as a dotted horizontal line. The green shaded region represents the unexplored regime in the high-spatial resolution image. The BSC corresponds to the integration of P_{aligned} over this shaded region.

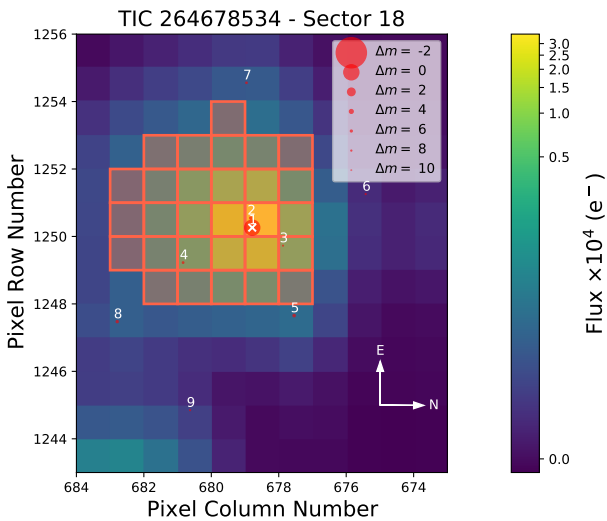


Fig. 3. Target pixel file of TESS for HD 207897 corresponding to sector 18, created with `tpfplotter` (Aller et al. 2020). The red square is related to the SPOC aperture mask, and red circles indicate the Gaia DR2 magnitude of nearby stars with the size depending on their brightness. HD 207897, number 1, has a *Gaia*(mag) = 8.1, while the nearest star, TIC 264678535, number 2, has a *Gaia*(mag) = 13.8.

magnitude and separation. In this case, given the AstraLux high-resolution image, we obtained a probability of an undetected blended source of 0.041%. We consider this probability low and the odds that such an undetected source might be an appropriate binary capable of mimicking the transit signal to be negligible. In addition, by using `tpfplotter` code⁸ (Aller et al. 2020), we plotted the target pixel file from TESS for HD 207897 b (see Fig. 3). We searched for possible light contamination by considering the nearby stars TIC 264678535 ($T_{\text{mag}} = 13.3$), TIC 264678538 ($T_{\text{mag}} = 15.69$) and TIC 264678529 ($T_{\text{mag}} = 14.39$),

which all lie inside the selected apertures analyzed by PDC-SAP. Because the *Gaia* *G* bandpass is quite similar to the TESS bandpass, we used the *Gaia* fluxes of these stars and estimated the level of contamination. The total flux due to nearby stars was only 0.8% of the HD 207897 flux, which is automatically corrected by SPOC. Because the probability of undetected blended sources from the AstraLux high-resolution image is low, the amount of light contamination due to nearby stars is negligible, and because similar Keplerian amplitudes were derived with different masks (see Sect. 3.3.1), we conclude that the transit and RV variations originate from the main target within the TESS TPF (HD 207897) and are of planetary origin.

3. Analysis and results

3.1. Stellar parameters

To obtain the stellar atmospheric parameters, we first summed the 66 spectra of SOPHIE after correcting for RV variations of the star, for barycentric Earth radial velocity, and correcting for the background of the calibration lamps (Hobson 2019). This resulted in a high S/N per pixel spectrum of 772 at 550 nm.

The T_{eff} and [Fe/H] were calculated following the procedure described in Santos et al. (2013) and Sousa et al. (2018). The procedure is based on the equivalent width of the Fe I and Fe II lines and assumes a balance in excitation and ionization of iron lines in local thermal equilibrium. The abundances of Mg and Si were derived by closely following the curve-of-growth analysis methods described in our previous works (Adibekyan et al. 2012, 2015). The abundances of C and O are very difficult to determine for stars cooler than about 5200 K (Delgado Mena et al. 2010; Bertran de Lis et al. 2015). We estimated the abundances of these elements empirically by using a machine-learning algorithm (we used the estimator RandomForestRegressor) from the Python Scikit-learn package (Pedregosa et al. 2011). The estimation of C and O was based on the abundance of Mg and Fe (Delgado Mena et al. 2017). Our initial sample was based on the HARPS sample, for which abundances of Mg and Fe are available (Adibekyan et al. 2012). Then we derived the O abundance for 535 stars and the C abundance for 758 stars following the method described in our previous works (Delgado Mena et al. 2010; Bertran de Lis et al. 2015). These samples were used as training and test datasets. The resulting abundances and other stellar parameters of HD 207897 are presented in Table 1.

As an independent stellar classification analysis, we used the FIES and TRES data following (SPC; Buchhave et al. 2012, 2014). The FIES analysis uses five spectral orders spanning a wavelength range from 5065 to 5320 Å, and the TRES analysis uses three spectral orders spanning the range from 5060 to 5300 Å. The spectra were compared to a library of synthetic templates to measure the effective temperature T_{eff} , surface gravity $\log g$, projected rotational velocity $v \sin i$, and metallicity [m/H] (a solar mix of metals). We analyzed the spectra individually and calculated a weighted average of each parameter. The results were $T_{\text{eff}} = 5085 \pm 50 \text{ K}$, $\log g = 4.48 \pm 0.10$, $v \sin i < 2 \text{ km s}^{-1}$, and [m/H] = -0.23 ± 0.08 , which agrees with the results of the other methods.

We also performed an analysis of the broadband spectral energy distribution (SED) of the star together with the *Gaia* EDR3 parallax (with no systematic offset applied; see, e.g., Stassun & Torres 2021), in order to determine an empirical measurement of the stellar radius, following the procedures described in Stassun & Torres (2016); Stassun et al. (2017a,b). We pulled the $B_T V_T$ magnitudes from *Tycho-2*, the *JHK_S*

⁸ <https://github.com/jlillo/tpfplotter>

Table 1. Stellar properties of HD 207897.

Other identifiers		
	TIC 264678534	
	HD 207897	
	BD +83 617	
	HIP 107038	
	<i>Gaia</i> DR2 2300641567596591488	
	2MASS J21404490+8420005	
Parameter	HD 207897	References
Astrometric properties		
Parallax (mas)	35.3446 ± 0.0468	<i>Gaia</i> DR2 ^(*)
	35.3581 ± 0.0159	<i>Gaia</i> EDR3
Distance	28.25 ± 0.03	<i>Gaia</i> DR2
α (hms)	21 : 40 : 44.78	<i>Gaia</i> DR2
δ (dms)	+84 : 20 : 00.56	<i>Gaia</i> DR2
Photometric properties		
<i>B</i> – <i>V</i>	0.86 ± 0.02	HIP
<i>V</i> (mag)	8.37 ± 0.0015	HIP
<i>Gaia</i> (mag)	8.1304 ± 0.0004	<i>Gaia</i> DR2
<i>Gaia</i> _{BP} (mag)	8.6051 ± 0.0025	<i>Gaia</i> DR2
<i>Gaia</i> _{RP} (mag)	7.5402 ± 0.0014	<i>Gaia</i> DR2
TESS(mag)	7.58 ± 0.006	TESS
<i>J</i> (mag)	6.830 ± 0.023	2MASS
<i>H</i> (mag)	6.391 ± 0.034	2MASS
<i>K</i> _s (mag)	6.312 ± 0.026	2MASS
<i>W</i> ₁ (mag)	6.262 ± 0.088	WISE
<i>W</i> ₂ (mag)	6.219 ± 0.025	WISE
<i>W</i> ₃ (mag)	6.275 ± 0.015	WISE
<i>W</i> ₄ (mag)	6.233 ± 0.045	WISE
Spectroscopic properties		
Spectral type	K0V	HIP
ξ_t (km s ^{−1})	0.53 ± 0.10	Sect. 3.1
$\log(R'_{HK})$	-4.83 ± 0.10	Sect. 3.3.2
$v \sin i$ (km s ^{−1})	< 2	Sect. 3.3.2
[Fe/H] dex	-0.21 ± 0.02	Sect. 3.1
[C/H] dex	-0.23 ± 0.07	Sect. 3.3.2
[O/H] dex	-0.11 ± 0.08	Sect. 3.3.2
[Mg/H] dex	-0.17 ± 0.06	Sect. 3.3.2
[Si/H] dex	-0.19 ± 0.05	Sect. 3.3.2
Bulk properties		
Mass (<i>M</i> _{sun})	$0.80^{+0.036}_{-0.030}$	Sect. 3.4
	0.84 ± 0.05	Sect. 3.1
Radius(<i>R</i> _{sun})	$0.779^{+0.019}_{-0.018}$	Sect. 3.4
	0.785 ± 0.014	Sect. 3.1
$\log g$ (cgs)	$4.559^{+0.026}_{-0.025}$	Sect. 3.4
<i>L</i> _s (<i>L</i> _{sun})	$0.360^{+0.019}_{-0.014}$	Sect. 3.4
<i>T</i> _{eff} (K)	5070^{+60}_{-57}	Sect. 3.4
<i>P</i> _{rot} (days)	37 ± 7	Sect. 3.3.2

Notes. ^(*)We applied the offset correction as prescribed in Lindegren et al. (2018).

magnitudes from 2MASS, the *W*₁–*W*₄ magnitudes from WISE, the *GG*_{BP}*G*_{RP} magnitudes from *Gaia*, and the NUV magnitude from GALEX. Together, the available photometry spans the full stellar SED over the wavelength range 0.2–22 μ m (see Fig. 4).

We performed a fit using Kurucz stellar atmosphere models, with the effective temperature (*T*_{eff}), metallicity ([Fe/H]), and

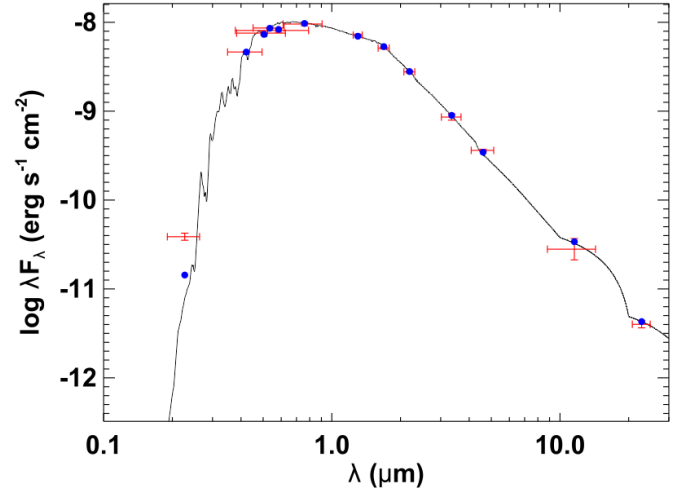


Fig. 4. Spectral energy distribution of HD 207897. Red symbols represent the observed photometric measurements, where the horizontal bars represent the effective width of the passband. Blue symbols are the model fluxes from the best-fit Kurucz atmosphere model (black).

surface gravity ($\log g$) adopted from the spectroscopic analysis. We also fixed the extinction $A_V \equiv 0$ based on the proximity of the stars (see Table 1). The resulting fit (Fig. 4) has a reduced χ^2 of 1.1, excluding the GALEX NUV flux, which indicates a moderate level of activity. When the (unreddened) model SED is integrated, the bolometric flux at Earth is $F_{\text{bol}} = 1.401 \pm 0.016 \times 10^{-8} \text{ erg s}^{-1} \text{ cm}^{-2}$. The F_{bol} and T_{eff} together with the *Gaia* parallax results in the stellar radius, $R_{\star} = 0.785 \pm 0.014 R_{\odot}$. In addition, we can estimate the stellar mass from the empirical relations of Torres et al. (2010), giving $M_{\star} = 0.84 \pm 0.05 M_{\odot}$. Additionally, we cross-checked these values with a different method by EXOFASTv2 in Sect. 3.4.

3.2. Photometry data analysis

The photometry was extracted with the pre-search data-conditioned simple aperture photometry (PDC-SAP) pipeline (Stumpe et al. 2012; Stumpe et al. 2014; Smith et al. 2012) provided by the TESS team. We removed nans and flagged low-quality data and 5σ outliers. We then normalized and detrended the light curve with a spline-robust iterative sigma-clipping method (Schoenberg 1946) using the Wotan package (Hippke et al. 2019)⁹. This method detrends the light curve by fitting the spline through minimizing the sum of squared residuals along with iteratively sigma-clipping. This step is one of the most important steps in the photometric analysis as it reduces the number of false-positive signals by removing instrumental and stellar noise. On the other hand, these detrending algorithms always include the risk of changing the transit depth or even fully remove shallow transits. For this reason, we tested different values of knots and chose the value of 0.7, which was the highest value that appeared suitable for removing the light-curve variabilities. The resulting light curve is shown in Fig. 5, and the transit events are marked with red triangles.

To search for any periodic signals in the data, we used the transit least-squares (TLS) algorithm (Hippke & Heller 2019), a method for investigating planetary transits that takes the stellar limb-darkening (Mandel & Agol 2002) and the effects of

⁹ <https://github.com/hippke/wotan>

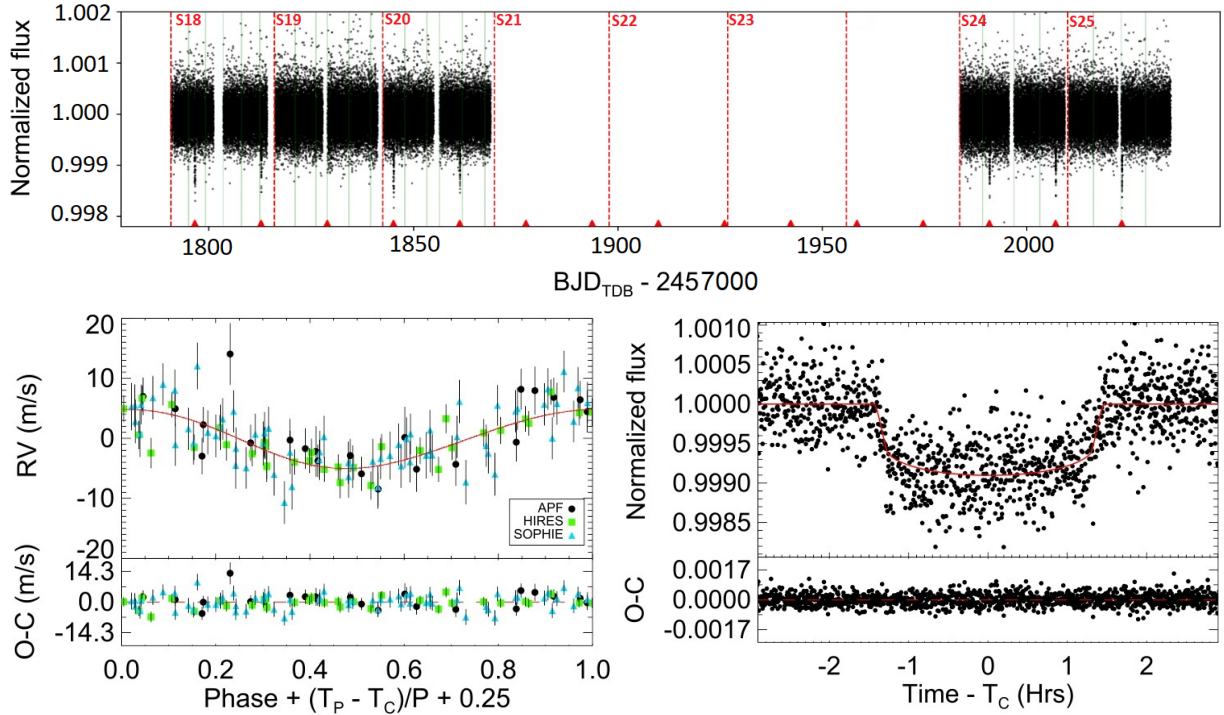


Fig. 5. TESS light curves and EXOFASTv2 best-fit models for RVs and photometric data. *Top panel:* full PDC-SAP (two-minute) TESS light curve after detrending, taken from sectors 18, 19, 20, 25, and 26. The red triangles indicate the transit events, and the green vertical lines indicate the momentum dumps of the spacecraft, which occur every 2.5 days. None of the transit events occurred during momentum dumps. *Bottom left:* phase-folded SOPHIE, APF, and HIRES RVs of HD 207897 b at the period of 16.20 d. *Bottom right:* TESS phase-folded light curve.

planetary ingress and egress into account. This method is publicly available¹⁰ and has been optimized for the signal detection efficiency (SDE) of small planets. We searched for periodic signals in the range 0.6–122 d and sampled 28607 periods within this range. The result showed a prominent periodic signal that occurred every 16.20 d with an S/N of 43, an SDE of 76.2 and a false-alarm probability (FAP) lower than 0.01% (see Fig. B.1). After masking the signal at 16.20 d, we ran the TLS again and did not see any periodic signals. A search for a long period beyond 122 d did not show any significant signals either.

3.3. Radial velocity data analysis

3.3.1. RV data reduction on SOPHIE

The SOPHIE data were reduced with the SOPHIE data reduction pipeline (DRS, Bouchy et al. 2009), which extracts the RV by cross-correlating spectrum with a binary mask and then fits a Gaussian of the cross-correlation function (CCF) (Pepe et al. 2002). We tested different masks, including G2, K0, and K5. Because they showed similar Keplerian amplitude variations, it is unlikely that these variations are produced by blend scenarios composed of stars of different spectral types (Bouchy et al. 2008). We finally adopted the RV data derived with the K5 mask because it presented a smaller RV dispersion.

We subsequently excluded six RV points that did not reach the required quality: three points with a lower S/N than required $S/N_{550} > 50$, two points with moonlight pollution, and one point that was an outlier and resulted from an observation performed without simultaneous calibration. We corrected the remaining points for the charge transfer inefficiency (CTI) effect (Santerne et al. 2012). This correction ranged from 1.4 to 6 m s⁻¹ with a

mean RV correction of 2.1 m s⁻¹. We then removed the nightly drift of the telescope measured from the simultaneous Th-Ar or FP reference spectra. This correction also falls within the 0.1 to 9 m s⁻¹ range, with a mean RV of 2.1 m s⁻¹.

The next step was to remove a long-term drift of the zero-point due to the instrumental effect identified in SOPHIE RV data (Courcol et al. 2015; Hobson et al. 2018). To track this offset, so-called ‘constant’ stars were monitored each night. We combined these observations to build a time series of the RV master constant (see Courcol et al. 2015 for more details of the method). We then estimated the long-term zeropoint drift as a function of time for each observation night and subtracted it from the HD 207897 RV data. This correction is in the 0.2–6 m s⁻¹ range with a mean value of 3.3 m s⁻¹. Because we saw the effects of the long-term drift of the zeropoints on the bisector span of constant stars, we applied the same processes to the bisector of HD 207897 as well. The correction for bisector was between 4 and 11 m s⁻¹ with a mean value of 2 m s⁻¹. After these corrections were applied, the HD 207897 RVs were reduced from an original RMS of 6.2 m s⁻¹ to a final RMS of 4.9 m s⁻¹.

3.3.2. Stellar rotation and activity

To investigate the activity of the star, we used several indicators such as bisector span, CCF FWHM, chromatic RV index (CRX), $H\alpha$, and $\log(R'_{HK})$ from SOPHIE spectra. We also used the S-index from the HIRES spectra.

We obtained the bisector span and CCF FWHM from the SOPHIE data reduction system. The CRX was extracted using the SERVAL (Zechmeister et al. 2018) code. To compute the $H\alpha$ index, which measures the flux in the $H\alpha$ line, we followed the definitions of Boisse et al. (2011). To do this, we also applied

¹⁰ <http://github.com/hippke/tls>

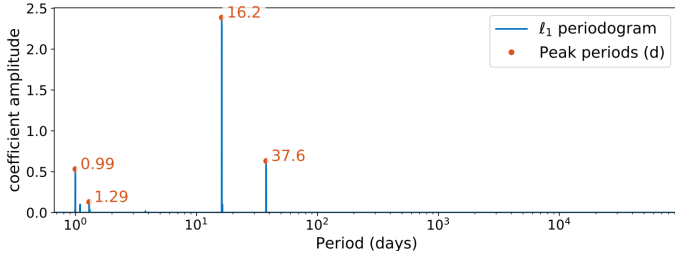


Fig. 6. ℓ_1 periodogram of SOPHIE RVs for HD 207897 b following Hara et al. (2017). The main peaks of the periodogram are indicated with orange circles.

background correction to the data as appropriate for the two different calibration lamps (for further details, see Hobson 2019).

We derived the S-index from HIRES spectra following Baliunas et al. (1995) and Paulson et al. (2002). We also computed the $\log(R'_{\text{HK}})$ index on SOPHIE spectra following the method of Noyes et al. (1984), but the S/N is low in all first (bluest) orders, where Ca H&K lines are located, with one exception in 2020 ($S/N = 33$). We decided to sum the bluest order of spectra with $S/N > 20$ to reach better S/Ns and then calculated $\log(R'_{\text{HK}})$. We first did this for the 2012–2015 spectra, of which 22 had an $S/N > 20$, giving a value of $\log(R'_{\text{HK}}) = -4.83 \pm 0.10$. Only one 2020 spectrum presents an $S/N > 20$, so that no summation was possible. This spectrum yields a value of $\log(R'_{\text{HK}}) = -4.78 \pm 0.10$, indicating that the star may have a similar level of activity as during the 2012–2015 period. Our value of $\log(R'_{\text{HK}})$ for 2012–2015 is consistent with $\log(R'_{\text{HK}}) = -4.86$ reported by Brewer et al. (2016). This value indicates a modest activity level of HD 207897.

To confirm our $\log(R'_{\text{HK}})$ value, we used the GALEX near-ultraviolet (NUV) flux excess of the star (Fig. 4). The observed NUV excess implies a chromospheric activity of $\log R'_{\text{HK}} = -4.82 \pm 0.05$ through the empirical relations of Findeisen et al. (2011), consistent with the value obtained spectroscopically. Moreover, the NUV-estimated activity implies an age of $\tau_* = 4.4 \pm 0.9$ Gyr according to the empirical relations of Mamajek & Hillenbrand (2008).

We estimated a stellar rotation period of 37 ± 7 d with the method proposed in Noyes et al. (1984), which agrees well with an estimated period of 36^{+5}_{-4} d following Mamajek & Hillenbrand (2008). These estimates are consistent with the value of 38 days from Isaacson & Fischer (2010).

We sought to constrain the P_{rot} of the star with RVs and activity indicators. We subtracted a linear drift in the CCF FWHM, CRX, and RVs time series, and a cubic drift in the S-index. Moreover, an offset term was fit on $H\alpha$ data between the two different calibration lamp background corrections (before and after BJD = 57284.4185). Then, we computed the periodogram of RVs, the RV-residuals of Keplerian models, and the activity indicators (Fig. 1). The RV residuals of planet b show two peaks at 35.9 and 37.6 days near the 10% FAP.

We ran an ℓ_1 periodogram on the RVs (see Fig. 6) for comparison. This was obtained with the same procedure as in Hara et al. (2020): we considered alternative noise models characterized by an autocovariance function that is a sum of white, correlated, and quasi-periodic components with different amplitudes and timescales and ranked them with cross-validation. The correlated component is a Gaussian kernel characterized by its timescale and amplitude, and the quasi-periodic component is a Gaussian kernel as in Haywood et al. (2014), characterized by its decay timescale, period, and amplitude. The

amplitudes of the white, correlated, and quasi-periodic terms were taken on a grid (0 to 3 m s^{-1} with a 0.5 m s^{-1} step), the timescales 0, 3, and 6 days for the correlated term, 30, 60, and 90 days for the quasi-periodic term, and 37.6 days for the period of the quasi-periodic component. We also included one offset per instrument in the base model. Figure 6 corresponds to the highest-ranked noise model. We found a significant signal at the planet period (FAP of 2×10^{-9}) and found a signal at 37.6 d with an FAP of 0.5. The signal at 37.6 d very likely corresponds to a stellar signal.

While the periodogram of the CCF FWHM and $H\alpha$ activity indicators does not exhibit any significant signals, CRX shows a peak near to 10% FAP at 36.5. The S-index periodogram shows several peaks at the long periods, but no correlation ($R = 0.16$) is found between the S-index and HIRES RVs. We note that given the relatively low value of $v \sin i$ ($2 \pm 1 \text{ km s}^{-1}$), we did not detect any correlations between the RVs and its residuals and bisector.

We searched the SAP and PDC-SAP light curves for a signal of the rational period of the star in the photometry. For this, we applied the systematics-insensitive periodogram (SIP) method¹¹ (Angus et al. 2016; Hedges et al. 2020) for SAP and the Gaussian process (GP) model on PDC-SAP light curves. The SIP method detrends the SAP light curve (see Fig. B.2 bottom) from TESS instrument systematics and also calculates the Lomb-Scargle periodogram and without requiring a predetrending of the light curves as other methods (e.g., the autocorrelation function, ACF, by McQuillan et al. 2013). This method was initially used for the Kepler mission and has recently been successfully applied for TESS data such as TOI-1259A (Martin et al. 2021) and TOI-700 (Hedges et al. 2020). The SIP periodogram (see Fig. B.2 top) does not exhibit any significant signal for HD 207897 b. We also applied a GP model on PDC-SAP light curves, but it did not display any convincing signal either.

To examine the origin of the 37.6 d signal further, following Hara et al. (2022), we investigated the phase and amplitude consistency of the 37.6-day signal in the SOPHIE RVs. We used the statistic defined in Eq. (14) of Hara et al. (2022). We fit an offset and a linear trend as well as a sinusoidal model for the 16.2-day planet. Adopting a value of the RV jitter of 3.16 m s^{-1} , we find that the hypothesis that the phase and amplitude of the 37.6-day signal is constant is rejected at 2σ . This further supports the hypothesis that this signal is due to activity.

Based on the estimated stellar rotational period value and the signal at the CRX activity indicator, it is likely that the signals at 35.9 and 37.6 days are due to the stellar rotation period. We take these peaks in our joint model analysis with EXOFASTv2 in Sect. 3.4 into account.

3.3.3. Radial velocity results

The combined RV data of HD 207897 are plotted in Fig. 7 after fitting a zeropoint offset for each RV dataset (see Table 2). We removed a linear trend of $-0.28 \pm 0.11 \text{ m s}^{-1} \text{ yr}^{-1}$ from RVs. We note that no notable differences were found in our results when this linear drift was included or excluded. However, because we saw a clear linear drift in the activity indicators such as the CCF FWHM and CRX, we decided to keep the drift.

We investigated the footprints of the planet in RVs by searching for periodic signals. To do this, we used the website of the Data and Analysis Center for Exoplanets (DACE, Delisle et al. 2016)¹² and computed periodograms for the RVs (Fig. 1).

¹¹ <https://github.com/christinahedges/TESS-SIP>

¹² Available at <https://dace.unige.ch>

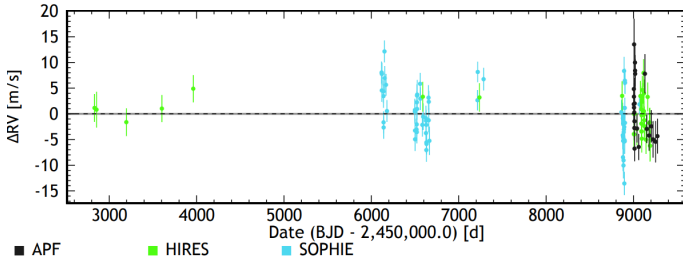


Fig. 7. Radial velocities of HD 207897 from SOPHIE, APF, and HIRES before correction for the linear trend.

The RV periodogram displays a clear peak at 16.20 d with a value lower than the 0.1% FAP (Baluev 2008). Moreover, the periodogram of activity indicators shows no corresponding peak. This shows that this periodic signal is likely due to a planet and not to stellar activity. See Fig. 1.

Figure 6 shows that the ℓ_1 periodogram confirms that the most prominent signal appears at 16.20 days with an FAP of 2×10^{-9} . The value of the second-highest peak at 37.7 days agrees with the estimated rotational period of the star (see Sect. 3.3.2).

3.4. Joint modeling of RV and photometry

To explore all the parameters of the system, including the host star and the planet, we simultaneously and self-consistently modeled the photometric observations of the star from five sectors of TESS and the RV observations from SOPHIE, HIRES, and APF using the fast exoplanetary fitting package (EXOFASTv2¹³, Eastman et al. 2013, 2019; Eastman 2017). This global modeling software uses a differential evolution Markov chain coupled with a Metropolis-Hastings Monte Carlo sampler that uses error scaling to explore the system parameters.

EXOFASTv2 fits a total of 33 free parameters for the HD 207897 system, which can be divided into the following categories:

- Twelve parameters related to the planet and activity period: the mid-transit time T_C , planet orbital period P , the ratio of the planet to star radius R_p/R_{star} (only for the planet), the orbital inclination i (only for the planet), the RV semi-amplitude K , and two more free parameters related to the eccentricity e .
- Two parameters for each RV instrument: instrumental offset and jitters. One free parameter is also fit for drift on RVs.
- Two limb-darkening coefficients for TESS photometric bandpasses, along with baseline flux and variance are fit for the transit light curve.
- Eleven stellar parameters: Stellar mass M_* , stellar radius R_* , and effective temperature T_{eff} by the MIST model, stellar radius $R_{*,\text{SED}}$ and effective temperature $T_{\text{eff},\text{SED}}$ by the SED model, observed metallicity $[\text{Fe}/\text{H}]$, theoretical metallicity at the star's birth $[\text{Fe}/\text{H}]_0$ by the MIST model, age, equivalent evolutionary point EPP, V-band extinction A_v , and distance d .

Before running EXOFASTv2, we set a Gaussian prior on T_{eff} and $[\text{Fe}/\text{H}]$ from our spectral analysis results, presented in Sect. 3.1. We also imposed a prior on the *Gaia* DR2 parallax after applying the offset correction as described in Lindgren et al. (2018). The broadband photometry presented in Table 1 is

also included. We enforced the upper limit for the V-band extinction (A_v) from Schlegel et al. (1998) and Schlafly & Finkbeiner (2011). The broadband photometry, the *Gaia* parallax, and A_v allowed us to model the stellar spectral energy distribution, which is key to constraining the stellar radius. EXOFASTv2 interpolates a precompiled 4D grid of bolometric corrections ($\log g$, T_{eff} , $[\text{Fe}/\text{H}]$, and reddening) to directly compute the broadband photometry flux. We did not set the limb darkening to let EXOFASTv2 constrain the best parameters of a quadratic limb darkening through the Claret (2017) tables for the TESS bands and the stellar atmosphere parameters (T_{eff} , $[\text{Fe}/\text{H}]$ index, and $\log g_*$). We used the Mesa isochrones and stellar tracks evolutionary model (MIST, Dotter 2016; Choi et al. 2016) to derive the full stellar parameters by combining our data. We also allowed the fitting of a linear slope on the original RVs as part of our joint analysis.

EXOFASTv2 considers the chains to be well mixed when the Gelman-Rubin statistic (Gelman et al. 2004, 1992; Ford 2006) decreases below 1.01. The Gelman-Rubin statistic describes how similar the chains are; a value under 1.01 shows that the chains are well mixed. The list of our priors and final median values of the posterior distributions together with their 1σ confidence intervals of the full system parameters are reported in Table 2.

As we showed in Sect. 3.3.2, HD 207897 has a moderate stellar activity and the signals at 35.9 and 37.6 d are likely to be due to the stellar rotation periods. Because these signals affect the mass estimate of the planet slightly, we considered them as an additional Keplerian fit in our global analysis. A more ideal solution to take activity into account is detrending the RVs using activity indicators (e.g., the S-index or the FWHM), but this is currently not possible with EXOFASTv2. Furthermore, we did not have the same activity indicators for all RVs for a detrending. As an independent analysis, we used only SOPHIE data and trained GP against CRX. The results agreed completely with the EXOFASTv2 global modeling. When we used two Keplerian models in EXOFASTv2, we did not fix the period and let EXOFASTv2 find the best activity period between the 35.9 and 37.6 d signals. After EXOFASTv2 converged, we saw a bimodality in the posterior distribution for the stellar activity periods (see Fig. 8, top). We therefore present the final median posterior distribution values of the two most probable solutions in Table 2. We also report their calculated probabilities based on the area of the posterior distributions. The probability of the most likely values is 54%, and that of the less likely values is 46%.

HD 207897 is a main-sequence K0 dwarf star. We found that its most likely values for mass is $0.800^{+0.036}_{-0.030} M_{\odot}$, for the radius, this value is $0.779^{+0.019}_{-0.018} R_{\odot}$, and for T_{eff} it is 5070^{+60}_{-57} K. These values agree well with the result of our stellar analysis in Sect. 3.1 and also with the stellar parameters from *Gaia* Data Release 2, such as $T_{\text{eff}} = 5052^{+114}_{-78}$ K and a radius of $0.79^{+0.80}_{-0.75} R_{\odot}$ (Brown et al. 2018).

We also show that the planet has a period of 16.20 d, a radius of $2.5 \pm 0.08 R_{\text{E}}$ and a mass of either $14.4 \pm 1.6 M_{\text{E}}$ or $15.9 \pm 1.6 M_{\text{E}}$ with nearly equal probability. These two solutions correspond to two possibilities for the stellar activity period. Hence, the density is either $5.1 \pm 0.7 \text{ g cm}^{-3}$ or $5.5^{+0.8}_{-0.7} \text{ g cm}^{-3}$. The two values agree with each other inside their error bars.

The Keplerian solution and transit model for HD 207897 b based on the most likely values are shown in Fig. 5 (bottom). The Keplerian model based on the most likely activity period of 37.6 d is illustrated in Fig. 8.

¹³ EXOFASTv2 is available at <https://github.com/jdeast/EXOFASTv2>

Table 2. Median values and 68% confidence interval for HD 207897 b and its host star.

Parameter	Units	Model priors	Activity on 35.9 d (Prob. = 46%)	Activity on 37.6 d (Prob. = 54%)
Stellar parameters:				
M_*	Mass (M_\odot)	—	$0.801^{+0.036}_{-0.031}$	$0.800^{+0.036}_{-0.030}$
R_*	Radius (R_\odot)	—	$0.779^{+0.019}_{-0.018}$	$0.779^{+0.019}_{-0.018}$
$R_{*,\text{SED}}$	Radius ⁽¹⁾ (R_\odot)	—	$0.7691^{+0.011}_{-0.0098}$	$0.7692^{+0.011}_{-0.010}$
L_*	Luminosity (L_\odot)	—	$0.360^{+0.019}_{-0.014}$	$0.360^{+0.019}_{-0.014}$
F_{Bol}	Bolometric Flux (cgs)	—	$0.00000001440^{+0.00000000076}_{-0.00000000056}$	$0.00000001439^{+0.00000000077}_{-0.00000000055}$
ρ_*	Density (cgs)	—	$2.39^{+0.19}_{-0.18}$	$2.39^{+0.19}_{-0.18}$
$\log g$	Surface gravity (cgs)	—	$4.558^{+0.027}_{-0.025}$	$4.559^{+0.026}_{-0.025}$
T_{eff}	Effective Temperature (K)	$\mathcal{N}[5012, 80]$	5071^{+57}_{-57}	5070^{+60}_{-57}
$T_{\text{eff, SED}}$	Effective Temperature ⁽¹⁾ (K)	—	5096^{+78}_{-54}	5096^{+78}_{-54}
[Fe/H]	Metallicity (dex)	$\mathcal{N}[-0.21, 0.08]$	$-0.040^{+0.037}_{-0.040}$	$-0.042^{+0.038}_{-0.041}$
[Fe/H] ₀	Initial Metallicity ⁽²⁾	—	$-0.028^{+0.050}_{-0.052}$	$-0.030^{+0.050}_{-0.053}$
Age	Age (Gyr)	—	$7.1^{+4.5}_{-4.4}$	7.1 ± 4.5
EEP	Equal Evolutionary Phase ⁽³⁾	—	343^{+17}_{-26}	343^{+17}_{-27}
A_V	V-band extinction (mag)	$\mathcal{U}[0, 0.3534]$	$0.074^{+0.081}_{-0.052}$	$0.074^{+0.081}_{-0.052}$
σ_{SED}	SED photometry error scaling	—	$2.10^{+0.77}_{-0.47}$	$2.10^{+0.77}_{-0.48}$
ϖ	Parallax (mas)	$\mathcal{N}[35.345, 0.047]$	$35.345^{+0.048}_{-0.047}$	35.345 ± 0.047
d	Distance (pc)	—	28.292 ± 0.038	28.293 ± 0.038
$\dot{\gamma}$	RV slope ⁽⁴⁾ ($\text{m s}^{-1}/\text{day}$)	—	-0.00078 ± 0.00030	$-0.00077^{+0.00027}_{-0.00028}$
Planetary parameters:				
P	Period (days)	—	16.202157 ± 0.000085	$16.202159^{+0.000085}_{-0.000083}$
R_P	Radius (R_E)	—	$2.505^{+0.081}_{-0.077}$	$2.501^{+0.082}_{-0.078}$
M_P	Mass (M_E)	—	15.9 ± 1.6	14.4 ± 1.6
T_C	Time of conjunction ⁽⁵⁾ (BJD _{TDB})	—	$2458926.10942^{+0.00047}_{-0.00049}$	$2458926.10942^{+0.00047}_{-0.00048}$
T_T	Time of minimum projected separation ⁽⁶⁾ (BJD _{TDB})	—	$2458926.10944^{+0.00047}_{-0.00047}$	$2458926.10943^{+0.00047}_{-0.00048}$
T_0	Optimal conjunction Time ⁽⁷⁾ (BJD _{TDB})	—	$2458926.10942^{+0.00047}_{-0.00049}$	$2458926.10942^{+0.00047}_{-0.00048}$
a	Semi-major axis (AU)	—	$0.1164^{+0.0017}_{-0.0015}$	$0.1163^{+0.0017}_{-0.0015}$
i	Inclination (Degrees)	—	$88.755^{+0.067}_{-0.066}$	88.757 ± 0.067
e	Eccentricity	—	$0.047^{+0.053}_{-0.033}$	$0.047^{+0.057}_{-0.033}$
ω_*	Argument of Periastron (Degrees)	—	-125^{+68}_{-95}	-100 ± 110
T_{eq}	Equilibrium temperature ⁽⁸⁾ (K)	—	$632.3^{+8.2}_{-7.0}$	$632.2^{+8.1}_{-7.0}$
τ_{circ}	Tidal circularization timescale (Gyr)	—	38700^{+8900}_{-7900}	35300^{+8300}_{-7300}
K	RV semi-amplitude (m s^{-1})	—	4.65 ± 0.45	4.24 ± 0.45
R_P/R_*	Radius of planet in stellar radii	—	$0.02946^{+0.00048}_{-0.00044}$	$0.02943^{+0.00049}_{-0.00046}$
a/R_*	Semi-major axis in stellar radii	—	$32.12^{+0.85}_{-0.82}$	$32.13^{+0.85}_{-0.82}$
δ	Transit depth (fraction)	—	$0.000868^{+0.000029}_{-0.000026}$	$0.000866^{+0.000029}_{-0.000027}$
Depth	Flux decrement at mid transit	—	$0.000868^{+0.000029}_{-0.000026}$	$0.000866^{+0.000029}_{-0.000027}$
τ	Ingress/egress transit duration (days)	—	$0.00684^{+0.00010}_{-0.00072}$	$0.00678^{+0.00011}_{-0.00077}$
T_{14}	Total transit duration (days)	—	$0.1214^{+0.0014}_{-0.0013}$	$0.1213^{+0.0014}_{-0.0013}$
T_{FWHM}	FWHM transit duration (days)	—	$0.1145^{+0.0012}_{-0.0011}$	$0.1145^{+0.0012}_{-0.0011}$
b	Transit Impact parameter	—	$0.712^{+0.041}_{-0.039}$	$0.709^{+0.043}_{-0.042}$
b_S	Eclipse impact parameter	—	$0.687^{+0.035}_{-0.047}$	$0.689^{+0.036}_{-0.048}$
τ_S	Ingress/egress eclipse duration (days)	—	$0.00640^{+0.00066}_{-0.00069}$	$0.00644^{+0.00070}_{-0.00071}$
$T_{S,14}$	Total eclipse duration (days)	—	$0.1208^{+0.0016}_{-0.0019}$	$0.1209^{+0.0018}_{-0.0019}$
$T_{S,\text{FWHM}}$	FWHM eclipse duration (days)	—	0.1143 ± 0.0015	0.1143 ± 0.0016
$\delta_{S,2.5\mu\text{m}}$	Blackbody eclipse depth at $2.5\mu\text{m}$ (ppm)	—	$0.205^{+0.026}_{-0.021}$	$0.204^{+0.026}_{-0.021}$
$\delta_{S,5.0\mu\text{m}}$	Blackbody eclipse depth at $5.0\mu\text{m}$ (ppm)	—	$7.09^{+0.50}_{-0.45}$	$7.07^{+0.50}_{-0.45}$
$\delta_{S,7.5\mu\text{m}}$	Blackbody eclipse depth at $7.5\mu\text{m}$ (ppm)	—	$20.2^{+1.1}_{-1.0}$	$20.2^{+1.1}_{-1.0}$
ρ_P	Density (cgs)	—	5.52 ± 0.73	5.05 ± 0.69
$\log g_P$	Surface gravity	—	3.393 ± 0.051	3.353 ± 0.053
Θ	Safronov Number	—	0.0647 ± 0.0067	0.0589 ± 0.0066
$\langle F \rangle$	Incident Flux ($10^9 \text{ erg s}^{-1} \text{ cm}^{-2}$)	—	$0.0361^{+0.0019}_{-0.0016}$	$0.0361^{+0.0019}_{-0.0016}$
T_P	Time of Periastron (BJD _{TDB})	—	$2458916.2^{+3.4}_{-4.3}$	$2458917.0^{+4.5}_{-5.4}$
T_S	Time of eclipse (BJD _{TDB})	—	$2458934.08^{+0.25}_{-0.40}$	$2458934.18^{+0.30}_{-0.38}$
T_A	Time of Ascending Node (BJD _{TDB})	—	$2458921.93^{+0.22}_{-0.42}$	$2458922.00^{+0.25}_{-0.42}$
T_D	Time of Descending Node (BJD _{TDB})	—	$2458930.16^{+0.31}_{-0.26}$	$2458930.18^{+0.36}_{-0.27}$
V_c/V_e	—	—	$1.010^{+0.067}_{-0.034}$	$1.007^{+0.069}_{-0.039}$
$e \cos \omega_*$	—	—	$-0.012^{+0.024}_{-0.039}$	$-0.003^{+0.029}_{-0.037}$
$e \sin \omega_*$	—	—	$-0.011^{+0.034}_{-0.065}$	$-0.007^{+0.039}_{-0.066}$
$M_P \sin i$	Minimum mass (M_E)	—	15.8 ± 1.6	14.4 ± 1.6
M_P/M_*	Mass ratio	—	0.0000594 ± 0.0000058	0.0000540 ± 0.0000058

Notes. Gaussian priors are presented by $\mathcal{N}(a, b)$, where a and b are the mean and width, respectively. Likewise, the uniform prior is denoted by $\mathcal{U}(c, d)$, and c and d present bounds on the parameter. The two solutions correspond to two possibilities for the stellar activity period. The highlighted parameters present a difference exceeding 0.5σ between the two solutions. See Table 3 in Eastman et al. (2019) for a detailed description of all parameters. ⁽¹⁾This value ignores the systematic error and is for reference only. ⁽²⁾The metallicity of the star at birth. ⁽³⁾Corresponds to static points in a star's evolutionary history. See Sect. 2 in Dotter (2016). ⁽⁴⁾Reference epoch = 2456438.359500. ⁽⁵⁾Time of conjunction is commonly reported as the “transit time”. ⁽⁶⁾Time of minimum projected separation is a more correct “transit time”. ⁽⁷⁾Optimal time of conjunction minimizes the covariance between T_C and Period. ⁽⁸⁾Assumes no albedo and perfect redistribution.

Table 2. continued.

Parameter	Units	Model priors	Activity on 35.9 d (Prob. = 46%)	Activity on 37.6 d (Prob. = 54%)
d/R_*	Separation at mid transit	—	$32.6^{+2.1}_{-1.6}$	$32.5^{+2.2}_{-1.7}$
P_T	A priori non-grazing transit prob	—	$0.0298^{+0.0015}_{-0.0018}$	$0.0299^{+0.0017}_{-0.0019}$
$P_{T,G}$	A priori transit prob	—	$0.0316^{+0.0016}_{-0.0019}$	$0.0317^{+0.0018}_{-0.0020}$
P_S	A priori non-grazing eclipse prob	—	$0.0307^{+0.0021}_{-0.0015}$	$0.0306^{+0.0022}_{-0.0016}$
$P_{S,G}$	A priori eclipse prob	—	$0.0326^{+0.0023}_{-0.0016}$	$0.0325^{+0.0023}_{-0.0017}$
Stellar activity parameters:				
P_{Activity}	Period (days)	—	$35.923^{+0.069}_{-0.067}$	$37.627^{+0.55}_{-0.076}$
$T_{C,\text{activity}}$	Time of conjunction ⁽⁵⁾ (BJD _{TDB})	—	2458917.1 ± 2.2	$2458910.7^{+2.3}_{-2.6}$
e_{Activity}	Eccentricity	—	$0.14^{+0.13}_{-0.10}$	$0.15^{+0.13}_{-0.11}$
$\omega_{*,\text{activity}}$	Argument of Periastron (Degrees)	—	-127^{+98}_{-96}	33^{+94}_{-92}
K_{Activity}	RV semi-amplitude (m s ⁻¹)	—	$2.38^{+0.51}_{-0.52}$	$2.25^{+0.50}_{-0.49}$
Telescope parameters for SOPHIE:				
γ_{rel}	Relative RV Offset ⁽⁴⁾ (m s ⁻¹)	—	-6327.36 ± 0.56	-6327.53 ± 0.52
σ_J	RV Jitter (m s ⁻¹)	—	$3.16^{+0.42}_{-0.37}$	$3.05^{+0.41}_{-0.37}$
σ_J^2	RV Jitter Variance	—	$10.0^{+2.8}_{-2.2}$	$9.3^{+2.7}_{-2.1}$
Telescope parameters for APF:				
γ_{rel}	Relative RV Offset ⁽⁴⁾ (m s ⁻¹)	—	3.1 ± 1.1	$2.9^{+1.1}_{-1.0}$
σ_J	RV Jitter (m s ⁻¹)	—	$1.6^{+1.2}_{-1.6}$	$1.4^{+1.3}_{-1.4}$
σ_J^2	RV Jitter Variance	—	$2.7^{+5.5}_{-3.4}$	$2.0^{+5.4}_{-3.2}$
Telescope parameters for HIRES:				
γ_{rel}	Relative RV Offset ⁽⁴⁾ (m s ⁻¹)	—	$1.61^{+0.83}_{-0.86}$	$1.81^{+0.81}_{-0.76}$
σ_J	RV Jitter (m s ⁻¹)	—	$2.15^{+0.46}_{-0.38}$	$2.42^{+0.49}_{-0.40}$
σ_J^2	RV Jitter Variance	—	$4.6^{+2.2}_{-1.5}$	$5.9^{+2.6}_{-1.8}$
Wavelength parameters:				
			TESS	TESS
u_1	linear limb-darkening coeff	—	0.386 ± 0.046	$0.385^{+0.046}_{-0.047}$
u_2	quadratic limb-darkening coeff	—	0.188 ± 0.048	$0.189^{+0.047}_{-0.048}$
Transit parameters:				
			TESS UT 2019-10-10 (TESS)	TESS UT 2019-10-10 (TESS)
σ^2	Added Variance	—	$0.0000000244 \pm 0.0000000011$	$0.0000000244 \pm 0.0000000011$
F_0	Baseline flux	—	$0.9999796^{+0.00000022}_{-0.00000023}$	$0.9999796^{+0.00000022}_{-0.00000023}$

4. Internal structure

In order to characterize the internal structure of HD 207897 b, we performed a Markov chain Monte Carlo (MCMC) Bayesian analysis (Dorn et al. 2015) using the interior composition model introduced in Brugger et al. (2017), Mousis et al. (2020), and Acuña et al. (2021), which comprises three layers: a Fe-rich core, a silicate-rich mantle, and a water layer. With an input equilibrium temperature of 637 K, assuming an albedo of zero, the irradiance that HD 207897 b received is enough to present vapor and supercritical phases if water is found on its surface. Therefore we coupled an atmosphere-interior model that calculates the surface conditions and the contribution of the atmosphere to the total radius.

We considered two scenarios to obtain the interior structure of HD 207897 b: scenario 1, in which only the mass and radius of the planet are considered as inputs to the MCMC analysis (shown in Table 2), and scenario 2, in which the planetary mass and radius and the stellar Fe/Si and Mg/Si mole ratios (see Table 1) are the input data. To compute the Fe/Si and Mg/Si mole ratios with the stellar abundances, we followed the approach depicted in Brugger et al. (2017) and Sotin et al. (2007). We obtained Fe/Si = 0.74 ± 0.09 and Mg/Si = 1.11 ± 0.20 . The outputs of the MCMC analysis are the posterior distributions functions (PDF) of the core mass fraction (CMF), the water mass fraction (WMF), and the atmospheric parameters, which are the temperature at 300 bar, the planetary albedo, and the atmospheric thickness from transit pressure to 300 bar. We assume a

water-rich atmosphere. Table 3 shows the 1D, 1σ confidence intervals of the MCMC output parameters.

In the most general case (scenario 1), up to 31% of the mass of HD 207897 b can be in the form of a hydrosphere. It reaches supercritical or superionic phases at its base (Mazevet et al. 2019) with the most likely value of the mass. This value increases slightly with the less likely value, although both cases are consistent with a water-rich planet with a water mass fraction of 20–30%. The 1σ confidence interval limits the maximum CMF to 0.50 (see Fig. 9). In addition, a Fe-depleted planet (CMF=0) is possible but unlikely. Assuming a pure silicate interior, the WMF is found to be 2.2×10^{-5} in HD 207897 b, which corresponds to a pressure at the base of the hydrosphere of approximately 300 bar.

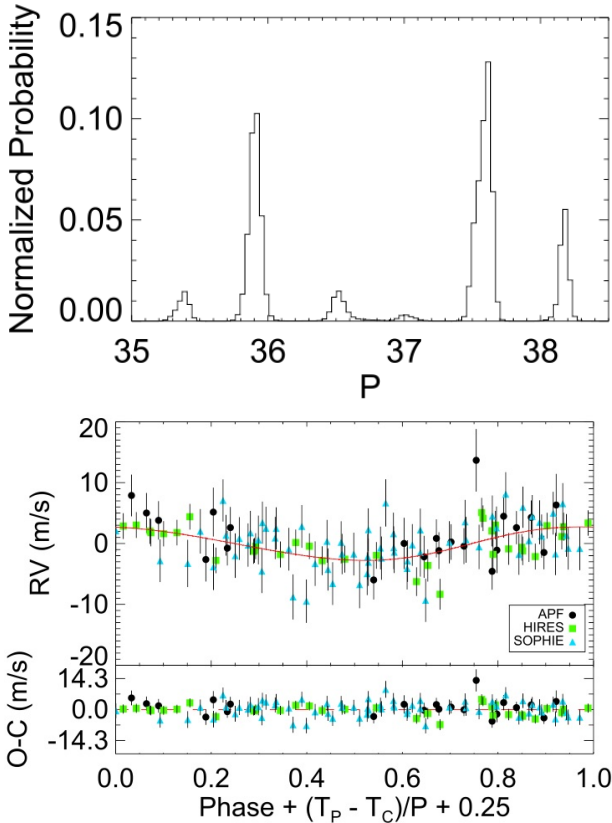
When we take the stellar abundances into account to constrain the planetary Fe/Si and Mg/Si mole ratios, the CMF is calculated to be 0.21, which is lower than the Earth's CMF (0.32). In this scenario, the WMF would be below 0.16, implying that HD 207897 b can be considered a water-rich planet. If the temperature and pressure of the hydrosphere are high enough to sustain a supercritical regime, then the atmosphere is extended and constitutes approximately 20% of the total planetary radius.

5. Discussion and summary

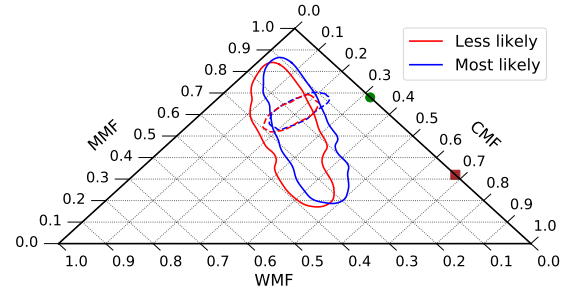
We detected and characterized a sub-Neptune orbiting HD 207897 with a period of 16.202161 ± 0.000083 d. We used TESS photometry data along with SOPHIE, HIRES, and

Table 3. 1σ confidence intervals of the interior and atmosphere MCMC output parameters in the two different compositional scenarios (see text).

Parameter	Activity on 37.6 d		Activity on 35.9 d	
	Scenario 1	Scenario 2	Scenario 1	Scenario 2
Core mass fraction, CMF	0.26 ± 0.18	0.19 ± 0.03	0.23 ± 0.18	0.19 ± 0.03
Water mass fraction, WMF	0.22 ± 0.09	0.19 ± 0.07	0.25 ± 0.10	0.21 ± 0.07
Temperature at 300 bar, T_{300} [K]	2715 ± 22		2742 ± 24	2737 ± 24
Thickness at 300 bar, z_{300} [km]	234 ± 22		265 ± 26	257 ± 25
Albedo, a_p	0.26 ± 0.01			
Core+Mantle radius, [R_p units]	0.72 ± 0.08	0.75 ± 0.05	0.70 ± 0.08	0.74 ± 0.05


Fig. 8. Bimodality in the posterior distribution for the stellar activity periods (*top*) and two-Keplerian model solution on the activity signal at 37.6 d with the initial period at 16.2 d (*bottom*).

APF RVs observations. We found that the planet has a radius of $2.5 \pm 0.08 R_E$ and a mass of either $14.4 \pm 1.6 M_E$ with a probability of 56% or $15.9 \pm 1.6 M_E$ with a probability of 46% based on bimodal results of the stellar activity period. The density accordingly translates into a high density of either $5.1 \pm 0.7 \text{ g cm}^{-3}$ or $5.5^{+0.8}_{-0.7} \text{ g cm}^{-3}$. We used the same mass and radii bounds as Otegi et al. (2020) from the NASA Exoplanet Data Archive¹⁴ (December 5, 2020) and plot all the sub-Neptune-sized planets ($2 < R/R_E < 4$) with a determined semimajor axis and luminosity in Fig. 10. This plot shows that HD 207897 b joins the group of dense sub-Neptunes such as HD 119130 b ($\rho_p = 7.4^{+1.6}_{-1.5} \text{ g cm}^{-3}$; Luque et al. 2019), GJ143 b ($\rho_p = 7^{+1.6}_{-1.3} \text{ g cm}^{-3}$; Dragomir et al. 2019), Kepler-10 c ($\rho_p = 7.1 \pm 1 \text{ g cm}^{-3}$; Dumusque et al. 2014), TOI-849 b ($\rho_p = 5.2^{+0.7}_{-0.8} \text{ g cm}^{-3}$; Armstrong et al. 2020), Kepler-538 b ($\rho_p = 5.4 \pm 1.3 \text{ g cm}^{-3}$; Mayo et al. 2019), Kepler-411 b


Fig. 9. 2D 1σ confidence regions of HD 207897 b for the mass estimation with activity period on 37.6 d (blue) and with activity period on 35.9 d (red). Solid lines indicate the confidence intervals of scenario 1, and dashed lines correspond to scenario 2, in which the stellar abundances are also included as input data in the MCMC interior structure analysis. The MMF is defined as $\text{MMF} = 1 - \text{CMF} - \text{WMF}$. The green dot and brown square indicate the position of Earth and Mercury in the ternary diagram, respectively.

($\rho_p = 9.9 \pm 1.3 \text{ g cm}^{-3}$; Sun et al. 2019), K2-110 b ($\rho_p = 5.2 \pm 1.2 \text{ g cm}^{-3}$; Osborn et al. 2017), and K2-263 b ($\rho_p = 5.7^{+1.6}_{-1.4} \text{ g cm}^{-3}$; Mortier et al. 2018). These planets are relatively close to their host stars and may have a similar formation history.

The question now is how HD 207897 b and other similar planets with such a high density can exist at a close distance to their host star. One possibility is that the planet has lost most of its volatile elements by evaporation, but for the case of HD 207897 b with an orbital period of 16.20 d and receiving an incident flux of $F = 26.3 F_E$, this is not a satisfactory answer. Even when we consider an extreme evaporation process (Lecavelier Des Étang 2007), the mass loss of the planet would be just $0.1 M_E$ during the entire lifetime of the star, which cannot account for its high density. HD 207897 b is unlikely to have formed in situ. According to Schlichting (2014), the maximum isolation mass that can form at a distance of $a = 0.12 \text{ AU}$ is only $\sim 0.06 M_E$ assuming a minimum mass solar nebula (MMSN). A disk surface density ~ 41 times higher than that of the solar nebula would be required to form a planet as massive as HD 207897 b at this distance. Two possible scenarios can be considered that are both consistent with the MMSN, however: Either the material from the outer region migrated and formed the planet HD 207897 b (e.g., Chatterjee & Tan 2013), or the formation of HD 207897 b occurred far away from the disk and the planet subsequently migrated to its current location (e.g., McNeil & Nelson 2010; Kley & Nelson 2012). The second scenario could have been triggered by another planet in this system. The hint of a long-term trend on RVs allows for the presence of another planet. The high occurrence rate of long-period giant planets (mass $> 0.3 M_J$) in systems harboring small planets

¹⁴ <https://exoplanetarchive.ipac.caltech.edu/>

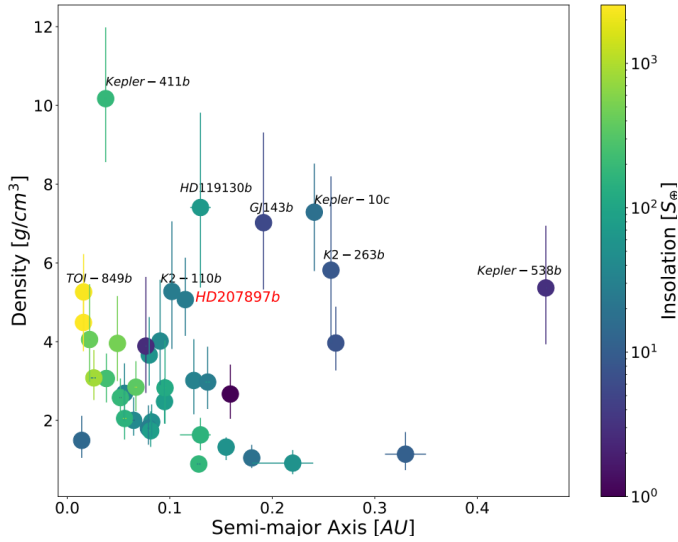


Fig. 10. Density-semimajor-axis diagram for HD 207897 b and other sub-Neptune-sized planets ($2 < R_E < 4$) with known semimajor axes, luminosity, and accurate mass and radius (Otegi et al. 2020). Dots are colored with planet insolation in Earth units ($S_p/S_\oplus = (L_*/L_\odot) \times (AU/a_p)^2$). The mentioned planets have a density higher than 5 g cm^{-3} .

(planets with masses or radii between those of Earth and Neptune) (Zhu & Wu 2018; Schlecker et al. 2021) can also support this scenario. In the case of HD 119130 b, Luque et al. (2019) suggested a migration scenario triggered by other planets to explain the linear drift in their RV data. However, more photometry and radial velocity observations are still needed to understand the planetary system HD 207897.

Furthermore, the brightness ($K = 6.3$ mag) of HD 207897, its relatively small stellar radius, and its quite nearby distance (28 pc) would make HD 207897 b a good target for atmospheric characterization. Similarly, the close distance and high brightness for a transiting planet host, make HD 207897 b an excellent target for studying the architecture of the system through ground-based observations. For example, measuring the host star spin-orbit alignment (obliquity) using the Rossiter-McLaughlin (RM, Rossiter 1924; McLaughlin 1924) anomaly can provide us with important information about planetary migration and evolution.

Acknowledgements. We warmly thank the OHP staff for their support on the observations. X.B., I.B. and T.F. received funding from the French Programme National de Physique Stellaire (PNPS) and the Programme National de Planétologie (PNP) of CNRS (INSU). We also acknowledge the financial support of French embassy in Tehran. N.H. acknowledges F. Vakili for his constant academic and administrative support. N.H. warmly thanks Ph. Stee, J. L. Beuzit, E. T. Givenchy for all their help. N.H. also thanks Jason D. Eastman and Michael Hippke who have written EXOFASTv2 and TLS package, respectively, for their guides. This publication makes use of The Data & Analysis Center for Exoplanets (DACE), which is a facility based at the University of Geneva (CH) dedicated to extrasolar planets data visualisation, exchange and analysis. DACE is a platform of the Swiss National Centre of Competence in Research (NCCR) PlanetS, federating the Swiss expertise in Exoplanet research. The DACE platform is available at <https://dace.unige.ch>. J.L.B. acknowledges financial support received from “la Caixa” Foundation (ID 100010434) and from the European Union’s Horizon 2020 research and innovation programme under the Marie Skłodowska-Curie grant agreement No 847648, with fellowship code LCF/BQ/PI20/11760023. This work has been carried out in the frame of the National Centre for Competence in Research “Planets” supported by the Swiss National Science Foundation (SNSF). This project has received funding from the European Research Council (ERC) under the European Union’s Horizon 2020 research and innovation programme (project SPICE DUNE, grant agreement No 947634). This work was supported by FCT – Fundação para a Ciência

e Tecnologia (FCT) through national funds and by FEDER through COMPETE2020 – Programa Operacional Competitividade e Internacionalização by these grants: UID/FIS/04434/2019; UIDB/04434/2020; UIDP/04434/2020; PTDC/FIS-AST/32113/2017 and POCI-01-0145-FEDER-032113; PTDC/FIS-AST/28953/2017 and POCI-01-0145-FEDER-028953. V.A., E.D.M., N.C.S., and S.G.S. also acknowledge the support from FCT through Investigador FCT contracts nr. IF/00650/2015/CP1273/CT0001, IF/00849/2015/CP1273/CT0003, IF/00169/2012/CP0150/CT0002, and IF/00028/2014/CP1215/CT0002, respectively, and POPH/FSE (EC) by FEDER funding through the program “Programa Operacional de Factores de Competitividade – COMPETE”. O.D.S.D. is supported in the form of work contract (DL 57/2016/CP1364/CT0004) funded by FCT. A.C. et P.C. acknowledge funding from the French National Research Agency (ANR) under contract number ANR-18-CE31-0019 (SPASH). N.A.D. acknowledges the support of FONDECYT project 3180063. S.H. acknowledges CNES funding through the grant 837319. X.D. and G.G. acknowledge funding in the framework of the Investissements d’Avenir program (ANR-15-IDEX-02), through the funding of the “Origin of Life” project of the Univ. Grenoble-Alpes. This work was supported by Fundação para a Ciência e a Tecnologia (FCT) and Fundo Europeu de Desenvolvimento Regional (FEDER) via COMPETE2020 through the research grants UIDB/04434/2020, UIDP/04434/2020, PTDC/FIS-AST/32113/2017 and POCI-01-0145-FEDER-032113, PTDC/FIS-AST/28953/2017 and POCI-01-0145-FEDER-028953. O.D.S.D. is supported in the form of work contract (DL 57/2016/CP1364/CT0004) funded by FCT. Resources supporting this work were provided by the NASA High-End Computing (HEC) Program through the NASA Advanced Supercomputing (NAS) Division at Ames Research Center for the production of the SPOC data products. Funding for the TESS mission is provided by NASA’s Science Mission directorate. We acknowledge the use of public TESS Alert data from pipelines at the TESS Science Office and at the TESS Science Processing Operations Center. This research has made use of the Exoplanet Follow-up Observation Program website, which is operated by the California Institute of Technology, under contract with the National Aeronautics and Space Administration under the Exoplanet Exploration Program. This paper includes data collected by the TESS mission that are publicly available from the Mikulski Archive for Space Telescopes (MAST). D.D. acknowledges support from the TESS Guest Investigator Program grant 80NSSC19K1727 and NASA Exoplanet Research Program grant 18-2XRP182-0136. T.D. acknowledges support from MIT’s Kavli Institute as a Kavli postdoctoral fellow. E.A.P. acknowledges the support of the Alfred P. Sloan Foundation. L.M.W. is supported by the Beatrice Watson Parrent Fellowship and NASA ADAP Grant 80NSSC19K0597. A.C. is supported by the NSF Graduate Research Fellowship, grant No. DGE 1842402. D.H. acknowledges support from the Alfred P. Sloan Foundation, the National Aeronautics and Space Administration (80NSSC19K0379), and the National Science Foundation (AST-1717000). I.J.M.C. acknowledges support from the NSF through grant AST-1824644. P.D. acknowledges support from a National Science Foundation Astronomy and Astrophysics Postdoctoral Fellowship under award AST-1903811. A.B. is supported by the NSF Graduate Research Fellowship, grant No. DGE 1745301. R.A.R. is supported by the NSF Graduate Research Fellowship, grant No. DGE 1745301. C.D.D. acknowledges the support of the Hellman Family Faculty Fund, the Alfred P. Sloan Foundation, the David and Lucile Packard Foundation, and the National Aeronautics and Space Administration via the TESS Guest Investigator Program (80NSSC18K1583). J.M.A.M. is supported by the NSF Graduate Research Fellowship, grant No. DGE-1842400. J.M.A.M. and P.C. acknowledge the LSSTC Data Science Fellowship Program, which is funded by LSSTC, NSF Cybertraining Grant No. 1829740, the Brinson Foundation, and the Moore Foundation; their participation in the program has benefited this work. This paper is partially based on observations made with the Nordic Optical Telescope, operated by the Nordic Optical Telescope Scientific Association at the Observatorio del Roque de los Muchachos, La Palma, Spain, of the Instituto de Astrofísica de Canarias.

References

- Acuña, L., Deleuil, M., Mousis, O., et al. 2021, *A&A*, **647**, A53
- Adibekyan, V. Z., Sousa, S. G., Santos, N. C., et al. 2012, *A&A*, **545**, A32
- Adibekyan, V., Figueira, P., Santos, N. C., et al. 2015, *A&A*, **583**, A94
- Aller, A., Lillo-Box, J., Jones, D., Miranda, L. F., & Forteza, S. B. 2020, *A&A*, **635**, A128
- Angus, R., Foreman-Mackey, D., & Johnson, J. A. 2016, *ApJ*, **818**, 109
- Armstrong, D. J., Lopez, T. A., Adibekyan, V., et al. 2020, *Nature*, **583**, 39
- Balunas, S. á., Donahue, R., Soon, W., et al. 1995, *ApJ*, **438**, 269
- Baluev, R. V. 2008, *MNRAS*, **385**, 1279
- Bertran de Lis, S., Delgado Mena, E., Adibekyan, V. Z., Santos, N. C., & Sousa, S. G. 2015, *A&A*, **576**, A89
- Bhatti, W., Bouma, L., Joshua, John, & Price-Whelan, A. 2020, waqasbhatti/astrobases: astrobases v0.5.0
- Boisse, I., Bouchy, F., Hébrard, G., et al. 2011, *A&A*, **528**, A4

- Borucki, W. J., Koch, D., Basri, G., et al. 2010, *Science*, **327**, 977
- Bouchy, F., Moutou, C., Queloz, D., et al. 2008, *Proc. Int. Astron. Union*, **4**, 129
- Bouchy, F., Hébrard, G., Udry, S., et al. 2009, *A&A*, **505**, 853
- Bouchy, F., Díaz, R., Hébrard, G., et al. 2013, *A&A*, **549**, A49
- Brewer, J. M., Fischer, D. A., Valenti, J. A., & Piskunov, N. 2016, *ApJS*, **225**, 32
- Brown, A., Vallenari, A., Prusti, T., et al. 2018, *A&A*, **616**, A1
- Brugger, B., Mousis, O., Deleuil, M., & Deschamps, F. 2017, *ApJ*, **850**, 93
- Buchhave, L. A., Bakos, G. Á., Hartman, J. D., et al. 2010, *ApJ*, **720**, 1118
- Buchhave, L. A., Latham, D. W., Johansen, A., et al. 2012, *Nature*, **486**, 375
- Buchhave, L. A., Bizzarro, M., Latham, D. W., et al. 2014, *Nature*, **509**, 593
- Burt, J., Hanson, R., Rivera, E., et al. 2014, *SPIE*, **9152**, 915211
- Butler, R. P., Marcy, G. W., Williams, E., et al. 1996, *PASP*, **108**, 500
- Chatterjee, S., & Tan, J. C. 2013, *ApJ*, **780**, 53
- Choi, J., Dotter, A., Conroy, C., et al. 2016, *ApJ*, **823**, 102
- Claret, A. 2017, *A&A*, **600**, A30
- Courcol, B., Bouchy, F., Pepe, F., et al. 2015, *A&A*, **581**, A38
- Delgado Mena, E., Israelian, G., González Hernández, J. I., et al. 2010, *ApJ*, **725**, 2349
- Delgado Mena, E., Tsantaki, M., Adibekyan, V. Z., et al. 2017, *A&A*, **606**, A94
- Delisle, J.-B., Ségransan, D., Buchschacher, N., & Alesina, F. 2016, *A&A*, **590**, A134
- Dorn, C., Khan, A., Heng, K., et al. 2015, *A&A*, **577**, A83
- Dotter, A. 2016, *ApJS*, **222**, 8
- Dragomir, D., Teske, J., Günther, M. N., et al. 2019, *ApJ*, **875**, L7
- Dumusque, X., Bonomo, A. S., Haywood, R. D., et al. 2014, *ApJ*, **789**, 154
- Eastman, J. 2017, Astrophysics Source Code Library [record ascl:1710.003]
- Eastman, J., Gaudi, B. S., & Agol, E. 2013, *PASP*, **125**, 83
- Eastman, J. D., Rodriguez, J. E., Agol, E., et al. 2019, *PASP*, submitted [arXiv:1907.09480]
- Findeisen, K., Hillenbrand, L., & Soderblom, D. 2011, *AJ*, **142**, 23
- Ford, E. B. 2006, *ApJ*, **642**, 505
- Fulton, B. J., Weiss, L. M., Sinukoff, E., et al. 2015, *ApJ*, **805**, 175
- Fulton, B. J., Petigura, E. A., Howard, A. W., et al. 2017, *AJ*, **154**, 109
- Fűrész, G. 2008, PhD thesis, University of Szeged, Hungary
- Gardner, J. P., Mather, J. C., Clampin, M., et al. 2006, *Space Sci. Rev.*, **123**, 485
- Gelman, A., & Rubin, D. B. 1992, *Stat. Sci.*, **7**, 457
- Gelman, A., Carlin, J. B., Stern, H. S., & Rubin, D. B. 2004, *CRC Texts in Statistical Science* (USA: CRC Press)
- Ginzburg, S., Schlichting, H. E., & Sari, R. 2016, *ApJ*, **825**, 29
- Ginzburg, S., Schlichting, H. E., & Sari, R. 2018, *MNRAS*, **476**, 759
- Girardi, L., Barbieri, M., Groenewegen, M. A. T., et al. 2012, *Astrophys. Space Sci. Proc.*, **26**, 165
- Günther, M. N., Pozuelos, F. J., Dittmann, J. A., et al. 2019, *Nat. Astron.*, **3**, 1099
- Hara, N. C., Boué, G., Laskar, J., & Correia, A. 2017, *MNRAS*, **464**, 1220
- Hara, N., Bouchy, F., Stalport, M., et al. 2020, *A&A*, **636**, L6
- Hara, N. C., Delisle, J.-B., Unger, N., & Dumusque, X. 2022, *A&A*, in press, <https://doi.org/10.1051/0004-6361/202141197>
- Haywood, R. D., Collier Cameron, A., Queloz, D., et al. 2014, *MNRAS*, **443**, 2517
- Hedges, C., Angus, R., Barentsen, G., et al. 2020, *Res. Notes AAS*, **4**, 220
- Hippke, M., & Heller, R. 2019, *A&A*, **623**, A39
- Hippke, M., David, T. J., Mulders, G. D., & Heller, R. 2019, *AJ*, **158**, 143
- Hobson, M. 2019, PhD thesis, Aix-Marseille, France
- Hobson, M., Díaz, R. F., Delfosse, X., et al. 2018, *A&A*, **618**, A103
- Hormuth, F., Brandner, W., Hippler, S., & Henning, T. 2008, *J. Phys. Conf. Ser.*, **131**, 012051
- Howard, A. W., Johnson, J. A., Marcy, G. W., et al. 2010, *ApJ*, **721**, 1467
- Huang, C. X., Vanderburg, A., Pál, A., et al. 2020a, *Res. Notes Am. Astron. Soc.*, **4**, 204
- Huang, C. X., Vanderburg, A., Pál, A., et al. 2020b, *Res. Notes Am. Astron. Soc.*, **4**, 206
- Isaacson, H., & Fischer, D. 2010, *ApJ*, **725**, 875
- Jenkins, J. M. 2002, *ApJ*, **575**, 493
- Jenkins, J. M., Chandrasekaran, H., McCaulliff, S. D., et al. 2010, *SPIE Conf. Ser.*, **7740**, 77400D
- Jenkins, J. M., Twicken, J. D., McCaulliff, S., et al. 2016, *SPIE*, **9913**, 99133E
- Kley, W., & Nelson, R. 2012, *ARA&A*, **50**, 211
- Lecavelier Des Étangs, A. 2007, *A&A*, **461**, 1185
- Li, J., Tenenbaum, P., Twicken, J. D., et al. 2019, *PASP*, **131**, 024506
- Lillo-Box, J., Barrado, D., & Bouy, H. 2012, *A&A*, **546**, A10
- Lillo-Box, J., Barrado, D., & Bouy, H. 2014, *A&A*, **566**, A103
- Lindgren, L., Hernández, J., Bombrun, A., et al. 2018, *A&A*, **616**, A2
- Lopez, E. D., & Fortney, J. J. 2014, *ApJ*, **792**, 1
- Luque, R., Nowak, G., Pallé, E., et al. 2019, *A&A*, **623**, A114
- Mamajek, E. E., & Hillenbrand, L. A. 2008, *ApJ*, **687**, 1264
- Mandel, K., & Agol, E. 2002, *ApJ*, **580**, L171
- Martin, D. V., El-Badry, K., Hodžić, V. K., et al. 2021, *MNRAS*, **507**, 4132
- Mayo, A. W., Rajpaul, V. M., Buchhave, L. A., et al. 2019, *AJ*, **158**, 165
- Mazevet, S., Licari, A., Chabrier, G., & Potekhin, A. Y. 2019, *A&A*, **621**, A128
- McLaughlin, D. 1924, *ApJ*, **60**
- McNeil, D., & Nelson, R. 2010, *MNRAS*, **401**, 1691
- McQuillan, A., Aigrain, S., & Mazeh, T. 2013, *MNRAS*, **432**, 1203
- Mink, D. J. 2011, *ASP Conf. Ser.*, **442**, 305
- Mortier, A., Bonomo, A., Rajpaul, V., et al. 2018, *MNRAS*, **481**, 1839
- Mousis, O., Deleuil, M., Agüichine, A., et al. 2020, *ApJ*, **896**, L22
- Nielsen, L. D., Gandolfi, D., Armstrong, D., et al. 2020, *MNRAS*, **492**, 5399
- Noyes, R., Hartmann, L., Baliunas, S., Duncan, D., & Vaughan, A. 1984, *ApJ*, **279**, 763
- Osborn, H., Santerne, A., Barros, S., et al. 2017, *A&A*, **604**, A19
- Otegi, J., Bouchy, F., & Helled, R. 2020, *A&A*, **634**, A43
- Owen, J. E., & Wu, Y. 2013, *ApJ*, **775**, 105
- Owen, J. E., & Wu, Y. 2017, *ApJ*, **847**, 29
- Paulson, D. B., Saar, S. H., Cochran, W. D., & Hatzes, A. P. 2002, *AJ*, **124**, 572
- Pedregosa, F., Varoquaux, G., Gramfort, A., et al. 2011, *J. Mach. Learn. Res.*, **12**, 2825
- Pepe, F., Mayor, M., Galland, F., et al. 2002, *A&A*, **388**, 632
- Perruchot, S., Kohler, D., Bouchy, F., et al. 2008, *SPIE*, **7014**, 70140J
- Ricker, G., Winn, J., Vanderspek, R., et al. 2015, *JATIS*, **1**, 014003
- Rogers, L. A. 2015, *ApJ*, **801**, 41
- Rossiter, R. 1924, *ApJ*, **60**, 15
- Santerne, A., Díaz, R., Moutou, C., et al. 2012, *A&A*, **545**, A76
- Santos, N., Sousa, S., Mortier, A., et al. 2013, *A&A*, **556**, A150
- Schlaflly, E. F., & Finkbeiner, D. P. 2011, *ApJ*, **737**, 103
- Schlecker, M., Mordasini, C., Emsenhuber, A., et al. 2021, *A&A*, **656**, A71
- Schlegel, D. J., Finkbeiner, D. P., & Davis, M. 1998, *ApJ*, **500**, 525
- Schlichting, H. E. 2014, *ApJ*, **795**, L15
- Schoenberg, I. J. 1946, *Q. Appl. Math.*, **4**, 112
- Smith, J. C., Stumpe, M. C., Van Cleve, J. E., et al. 2012, *PASP*, **124**, 1000
- Sotin, C., Grasset, O., & Mocquet, A. 2007, *Icarus*, **191**, 337
- Sousa, S., Adibekyan, V., Delgado-Mena, E., et al. 2018, *A&A*, **620**, A58
- Stassun, K. G., & Torres, G. 2016, *AJ*, **152**, 180
- Stassun, K. G., & Torres, G. 2021, *ApJ*, **907**, L33
- Stassun, K. G., Collins, K. A., & Gaudi, B. S. 2017a, *AJ*, **153**, 136
- Stassun, K. G., Corsaro, E., Pepper, J. A., & Gaudi, B. S. 2017b, *AJ*, **155**, 22
- Strehl, K. 1902, *Astron. Nachr.*, **158**, 89
- Stumpe, M. C., Smith, J. C., Van Cleve, J. E., et al. 2012, *PASP*, **124**, 985
- Stumpe, M. C., Smith, J. C., Catanzarite, J. H., et al. 2014, *PASP*, **126**, 100
- Sun, L., Ioannidis, P., Gu, S., et al. 2019, *A&A*, **624**, A15
- Telling, J. H., Avila, G., Buchhave, L., et al. 2014, *Astron. Nachr.*, **335**, 41
- Torres, G., Andersen, J., & Giménez, A. 2010, *A&ARv*, **18**, 67
- Twicken, J. D., Catanzarite, J. H., Clarke, B. D., et al. 2018, *PASP*, **130**, 064502
- Zechmeister, M., Reiners, A., Amado, P. J., et al. 2018, *A&A*, **609**, A12
- Zhu, W., & Wu, Y. 2018, *AJ*, **156**, 92

¹ Department of Physics, Shahid Beheshti University, Tehran, Iran

² Laboratoire J.-L. Lagrange, Observatoire de la Côte d'Azur (OCA), Université de Nice-Sophia Antipolis (UNS), CNRS, Campus Valrose, 06108 Nice Cedex 2, France

³ Aix Marseille Univ, CNRS, CNES, LAM, Marseille, France

⁴ Instituto de Astrofísica de Canarias, 38205 La Laguna, Tenerife, Spain

⁵ Departamento de Astrofísica, Universidad de La Laguna, 38206 La Laguna, Tenerife, Spain

⁶ Observatoire de Haute-Provence, CNRS, Université d'Aix-Marseille, 04870 Saint-Michel-l'Observatoire, France

⁷ Institut d'astrophysique de Paris, UMR 7095 CNRS université Pierre et Marie Curie, 98 bis, boulevard Arago, 75014 Paris, France

⁸ Observatoire de Genève, Université de Genève, Chemin Pegasi, 51, 1290 Sauverny, Switzerland

⁹ Centro de Astrobiología (CAB, CSIC-INTA), Depto. de Astrofísica, ESAC campus, 28692, Villanueva de la Cañada (Madrid), Spain

¹⁰ Center for Astrophysics | Harvard & Smithsonian, 60 Garden St, Cambridge, MA 02138, USA

¹¹ Canada France Hawaii Telescope Corporation (CFHT), 65-1238 Mamalahoa Hwy, Kamuela HI 96743 USA

¹² Departamento de Matemática y Física Aplicadas, Universidad Católica de la Santísima Concepción, Alonso de Rivera 2850, Concepción, Chile

¹³ Instituto de Astrofísica e Ciências do Espaço, Universidade do Porto, CAUP, Rua das Estrelas, 4150-762 Porto, Portugal

- ¹⁴ Departamento de Física e Astronomia, Faculdade de Ciências, Universidade do Porto, Rua do Campo Alegre, 4169-007 Porto, Portugal.
- ¹⁵ Univ. Grenoble Alpes, CNRS, IPAG, 38000 Grenoble, France
- ¹⁶ NASA Goddard Space Flight Center, 8800 Greenbelt Rd, Greenbelt, MD 20771, USA
- ¹⁷ University of Maryland, Baltimore County, 1000 Hilltop Cir, Baltimore, MD 21250, USA
- ¹⁸ Space Telescope Science Institute, 3700 San Martin Dr, Baltimore, MD 21218, USA
- ¹⁹ Division of Geological and Planetary Science, California Institute of Technology, Pasadena, CA 91125, USA
- ²⁰ Department of Physics & Astronomy, University of California Irvine, Irvine, CA 92697, USA
- ²¹ Department of Astronomy and Astrophysics, University of California, Santa Cruz, CA 95060, USA
- ²² Department of Physics & Astronomy, University of Kansas, 1082 Malott, 1251 Wescoe Hall Dr., Lawrence, KS 66045, USA
- ²³ Institute for Astronomy, University of Hawai'i, 2680 Woodlawn Drive, Honolulu, HI 96822, USA
- ²⁴ International Center for Advanced Studies (ICAS) and ICIFI (CON-ICET), ECyT-UNSAM, Campus Miguelete, 25 de Mayo y Francia, (1650) Buenos Aires, Argentina
- ²⁵ Department of Physics, and Kavli Institute for Astrophysics and Space Research, Massachusetts Institute of Technology, Cambridge, MA 02139, USA
- ²⁶ Department of Physics and Astronomy, University of New Mexico, 1919 Lomas Blvd NE, Albuquerque, NM 87131, USA
- ²⁷ Department of Astronomy, University of California Berkeley, Berkeley, CA, 94720, USA
- ²⁸ Division of Geological and Planetary Sciences 1200 E California Blvd, Pasadena, CA, 91125, USA
- ²⁹ Department of Earth and Planetary Sciences, University of California, Riverside, CA 92521, USA
- ³⁰ NASA Exoplanet Science Institute/Caltech-IPAC, MC 314-6, 1200 E. California Blvd., Pasadena, CA 91125, USA
- ³¹ Millennium Institute for Astrophysics, Chile
- ³² Instituto de Astrofísica, Facultad de Física, Pontificia Universidad Católica de Chile, Chile
- ³³ Department of Astronomy, California Institute of Technology, Pasadena, CA 91125, USA
- ³⁴ Kavli Institute for Particle Astrophysics and Cosmology, Stanford University, Stanford, CA 94305, USA
- ³⁵ Centre for Astrophysics, University of Southern Queensland, Toowoomba, QLD, Australia
- ³⁶ Department of Physics & Astronomy, University of California Los Angeles, Los Angeles, CA 90095, USA
- ³⁷ Las Campanas Observatory, Carnegie Institution of Washington, Colina el Pino, Casilla 601 La Serena, Chile
- ³⁸ Department of Physics and Astronomy, Johns Hopkins University, 3400 N Charles St, Baltimore, MD 21218, USA
- ³⁹ Gemini Observatory/NSF's NOIRLab, 670 N. A'ohoku Place, Hilo, HI 96720, USA
- ⁴⁰ LESIA, Observatoire de Paris, Université PSL, CNRS, Sorbonne Université, Université de Paris, 5 place Jules Janssen, 92195, Meudon, France
- ⁴¹ Univ. de Toulouse, CNRS, IRAP, 14 avenue Belin, 31400 Toulouse, France
- ⁴² Vanderbilt University, Department of Physics & Astronomy, 6301 Stevenson Center Ln., Nashville, TN 37235, USA
- ⁴³ SETI Institute/NASA Ames Research Center, USA
- ⁴⁴ DTU Space, National Space Institute, Technical University of Denmark, Elektrovej 328, 2800 Kgs. Lyngby, Denmark
- ⁴⁵ Department of Astrophysical Sciences, Princeton University, 4Ivy Lane, Princeton, NJ 08544, USA
- ⁴⁶ NASA Ames Research Center, Moffett Field, CA, 94035, USA
- ⁴⁷ Department of Physics, University of Warwick, Coventry, CV4 7AL, UK
- ⁴⁸ Centre for Exoplanets and Habitability, University of Warwick, Gibbet Hill Road, Coventry, CV4 7AL, UK
- ⁴⁹ Department of Earth, Atmospheric and Planetary Sciences, Massachusetts Institute of Technology, Cambridge, MA 02139, USA
- ⁵⁰ Department of Aeronautics and Astronautics, MIT, 77 Massachusetts Avenue, Cambridge, MA 02139, USA

Appendix A: RV time series

Table A.1: SOPHIE RVs for HD207897 b

BJD (-2400000 d)	RV (km s ⁻¹)	σ_{RV} (km s ⁻¹)	FWHM (km s ⁻¹)	BIS (km s ⁻¹)	H α	$\sigma_{H\alpha}$	CRX	σ_{CRX}
56117.5531	-6.3203	0.0015	6.6803	-0.0025	0.1294	0.0005	-39.0617	13.9761
56118.5849	-6.3205	0.0015	6.6846	0.0027	0.1305	0.0005	-34.4212	12.8526
56119.5401	-6.3238	0.0016	6.6849	-0.0016	0.1296	0.0006	-12.6147	12.0847
56120.5123	-6.3206	0.0016	6.6712	-0.0006	0.1306	0.0006	-29.3660	11.2578
56137.5869	-6.3240	0.0016	6.7125	0.0011	0.1323	0.0006	-36.7534	14.7557
56138.5331	-6.3249	0.0017	6.6945	0.0065	0.1335	0.0007	-28.7203	14.5124
56139.5731	-6.3300	0.0015	6.6839	-0.0008	0.1296	0.0005	32.8700	12.5074
56140.5330	-6.3310	0.0016	6.6906	0.0043	0.1310	0.0006	-34.3580	10.0305
56150.5049	-6.3162	0.0015	6.6867	-0.0028	0.1343	0.0005	-7.1528	14.0474
56152.5655	-6.3214	0.0018	6.6849	0.0002	0.1334	0.0008	-9.6228	14.1995
56167.5191	-6.3227	0.0015	6.6823	0.0054	0.1302	0.0006	-53.2894	10.1835
56178.3748	-6.3278	0.0015	6.7033	0.0013	0.1323	0.0006	-46.0315	12.8783
56497.5314	-6.3279	0.0018	6.6991	-0.0020	0.1288	0.0008	-27.5805	15.6965
56498.5527	-6.3276	0.0016	6.7072	0.0070	0.1326	0.0006	-6.9804	14.2738
56499.5446	-6.3316	0.0016	6.7074	-0.0023	0.1316	0.0006	-41.0561	12.8978
56500.5510	-6.3333	0.0017	6.6891	-0.0059	0.1321	0.0007	5.3262	13.2646
56517.4678	-6.3314	0.0016	6.7181	0.0051	0.1337	0.0007	15.8414	9.3975
56519.4789	-6.3304	0.0016	6.7067	-0.0048	0.1332	0.0007	-18.4473	11.5302
56520.4837	-6.3319	0.0016	6.7042	-0.0029	0.1345	0.0006	20.1748	12.7335
56521.4875	-6.3261	0.0016	6.6994	-0.0011	0.1338	0.0007	-12.2005	14.9481
56522.4818	-6.3248	0.0016	6.7130	0.0057	0.1331	0.0006	-9.6604	11.5639
56523.4905	-6.3274	0.0015	6.7106	0.0077	0.1319	0.0006	-36.2878	13.6435
56524.4789	-6.3246	0.0024	6.6754	0.0101	0.1384	0.0013	-0.9706	21.2910
56558.3761	-6.3225	0.0015	6.7002	-0.0020	0.1301	0.0006	-12.9535	15.0095
56560.3978	-6.3254	0.0016	6.7038	0.0003	0.1311	0.0006	-30.1229	14.8829
56583.3673	-6.3305	0.0017	6.6867	-0.0021	0.1307	0.0008	-6.3707	16.6035
56592.3536	-6.3289	0.0021	6.6841	-0.0077	0.1321	0.0011	-8.3097	21.0877
56624.3190	-6.3292	0.0019	6.7214	0.0091	0.1346	0.0009	6.39867	17.5343
56625.2867	-6.3321	0.0015	6.7172	-0.0040	0.1310	0.0006	17.7943	10.9701
56626.2718	-6.3297	0.0015	6.7156	0.0024	0.1327	0.0006	-3.3048	12.3435
56628.3163	-6.3305	0.0016	6.7214	0.0007	0.1322	0.0007	-8.6098	14.9817
56629.3041	-6.3354	0.0017	6.7138	-0.0064	0.1322	0.0007	11.1813	13.8973
56630.2650	-6.3339	0.0014	6.7173	0.0018	0.1304	0.0005	-11.7681	12.1465
56631.2725	-6.3342	0.0014	6.7182	-0.0030	0.1297	0.0005	-23.8070	12.1372
56654.2301	-6.3252	0.0019	6.7088	-0.0011	0.1349	0.0009	-15.5221	17.2095
56656.2313	-6.3296	0.0018	6.7171	0.0054	0.1324	0.0008	2.0870	14.7556
56657.2325	-6.3260	0.0015	6.7183	0.0059	0.1325	0.0006	21.1445	11.7855
56664.2359	-6.3336	0.0023	6.7235	0.0026	0.1303	0.0013	-9.4066	21.0183
57214.5707	-6.3257	0.0013	6.7541	-0.0027	0.1291	0.0005	4.0133	13.6434
57217.5644	-6.3202	0.0013	6.7651	0.0025	0.1284	0.0006	5.5657	16.3052
57284.4185	-6.3216	0.0016	6.7057	-0.0038	0.1293	0.0007	-3.4004	12.3004
58862.3082	-6.3280	0.0018	6.7636	0.0076	0.1415	0.0009	-1.5094	21.4660
58875.3024	-6.3284	0.0016	6.8431	-0.0004	0.1440	0.0007	108.6779	21.7024
58877.3789	-6.3325	0.0023	6.7005	0.0187	0.1470	0.0013	69.2134	29.4011
58878.3249	-6.3292	0.0019	6.7894	-0.000	0.1437	0.0009	57.8937	28.6864
58879.3132	-6.3368	0.0022	6.8407	-0.0178	0.1444	0.0011	54.4243	36.3337
58880.2542	-6.3327	0.0012	6.8466	0.0038	0.1414	0.0005	53.1909	18.2402
58881.2536	-6.3336	0.0016	6.7832	-0.0118	0.1455	0.0007	49.2682	15.8376
58882.6853	-6.3330	0.0025	6.7353	-0.0007	0.1445	0.0014	80.9618	43.6620
58883.2559	-6.3304	0.0017	6.7916	-0.0008	0.1442	0.0008	60.3972	18.5206
58885.2949	-6.3384	0.0020	6.7925	-0.0120	0.1415	0.0010	102.8511	29.6527
58886.2969	-6.3374	0.0017	6.8429	-0.0090	0.1438	0.0008	50.0756	21.1131
58888.2703	-6.3319	0.0016	6.8534	-0.0097	0.1424	0.0007	84.0189	25.1804
58890.2920	-6.3314	0.0023	6.7950	-0.0084	0.1472	0.0012	70.5820	30.6721
58892.2593	-6.3200	0.0023	6.7914	0.0029	0.1485	0.0012	61.7681	27.8826
58894.2567	-6.3309	0.0014	6.8221	-0.0060	0.1436	0.0006	85.0683	18.1804
58895.2570	-6.3419	0.0017	6.8537	0.0008	0.1447	0.0008	76.4210	22.0550
58898.2952	-6.3335	0.0021	6.7098	0.0081	0.1446	0.0012	-12.7695	29.9844
58899.2728	-6.3337	0.0019	6.7510	-0.0144	0.1441	0.0009	-4.7509	23.2686
58900.2705	-6.3272	0.0013	6.8566	-0.0026	0.1399	0.0005	17.5256	13.1316
58901.2780	-6.3219	0.0018	6.8054	0.0090	0.1453	0.0009	6.4814	19.9266
58902.2708	-6.3301	0.0012	6.8455	-0.0022	0.1419	0.0005	21.4611	14.2376
58903.2734	-6.3223	0.0016	6.8011	-0.0038	0.1415	0.0007	67.6199	20.3261
59068.5491	-6.3265	0.0011	6.6780	0.0011	—	—	—	—

Table A.2: HIRES RVs for HD207897 b

BJD (-2400000 d)	RV (m s ⁻¹)	σ_{RV} (m s ⁻¹)	S-index	$\sigma_{S-index}$
52832.039671	-6.1499	1.04	—	—
52855.027852	-6.4812	2.42	—	—
53196.053218	-8.9158	1.01	—	—
53602.917000	1.127055	0.819542	0.231000	0.001000
53962.008000	4.990706	0.870220	0.222000	0.001000
56588.935000	3.431498	1.463105	0.225000	0.001000
57237.106000	3.290118	1.190904	0.215400	0.001000
58869.707000	3.595136	1.360255	0.249000	0.001000
59004.080000	-3.829985	1.708751	0.251100	0.001000
59007.977000	0.107424	1.636860	0.247300	0.001000
59008.017000	0.038845	1.893359	0.249900	0.001000
59008.066000	-3.912803	1.738616	0.250000	0.001000
59039.084000	-2.874458	1.880687	0.240000	0.001000
59079.039000	3.561938	1.538733	0.238600	0.001000
59089.002000	0.991416	1.012931	0.233500	0.001000
59090.031000	-1.806837	0.977288	0.236100	0.001000
59091.056000	-3.314227	0.904606	0.233400	0.001000
59092.060000	-3.337441	0.963977	0.237100	0.001000
59093.027000	-0.185500	0.992191	0.239300	0.001000
59094.984000	-4.733336	0.983995	0.233400	0.001000
59097.973000	2.455004	1.046085	0.235400	0.001000
59099.827000	2.774576	1.035973	0.236600	0.001000
59100.985000	4.753109	1.043153	0.237800	0.001000
59102.009000	3.388690	0.992955	0.237100	0.001000
59115.059000	8.057584	0.990576	0.244300	0.001000
59118.985000	0.615674	1.028696	0.240700	0.001000
59119.868000	4.070617	1.021998	0.239300	0.001000
59120.980000	-0.036780	0.993603	0.241600	0.001000
59122.955000	-1.142312	0.922378	0.239500	0.001000
59123.937000	-2.279427	0.982050	0.238200	0.001000
59142.961000	-4.944806	1.161786	0.242200	0.001000
59153.887000	-2.863129	1.141554	0.240700	0.001000
59181.890000	-1.681638	1.441832	0.236500	0.001000
59187.825000	-1.590208	1.406428	0.227200	0.001000
59188.813000	-6.084715	1.833509	0.227800	0.001000
59189.870000	-6.143414	1.421509	0.229800	0.001000

Notes. The first three data were taken with a different CCD detector. For the sake of simplicity, we excluded them in our joint modeling by EXOFASTv2.

Table A.3: APF RVs for HD207897 b

BJD (-2400000 d)	RV (m s ⁻¹)	σ_{RV} (m s ⁻¹)
59002.885	3.030364933	3.218557358
59003.809	5.987553939	2.861260653
59004.916	4.500414023	2.633646965
59005.881	2.367894193	2.662182808
59006.804	14.66981698	4.979400635
59008.864	1.427995591	3.299036264
59009.826	-1.594891397	2.404323578
59010.938	-0.297586458	2.476657391
59011.895	-5.612035257	2.451689482
59012.812	3.174356114	4.957623482
59016.811	11.1418913	3.183858633
59017.938	9.565100481	3.032974005
59018.847	8.944296078	2.887774467
59039.912	-1.683343659	2.742200613
59059.929	-5.287302366	2.546239138
59130.705	8.958821818	3.813406229
59151.657	-1.77725919	2.748860359
59178.67	-3.064406035	2.962447405
59203.816	-1.276284674	3.144914389
59223.847	-3.812726288	3.542819262
59252.786	-4.278596616	4.021532536
59273.802	-3.184576312	3.384922504

Appendix B: Figures

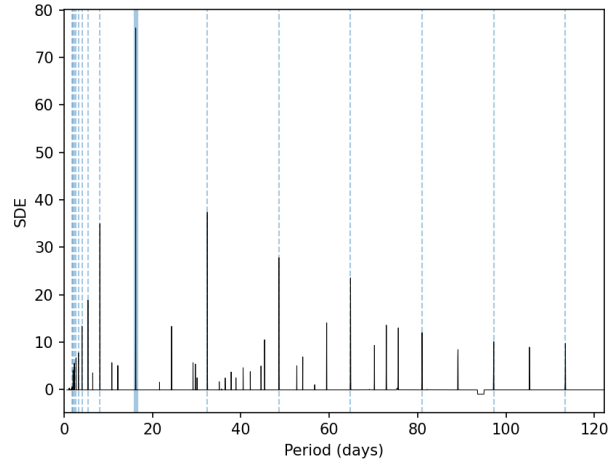


Fig. B.1: TLS periodogram for the TESS light curve of HD207897 b. The blue line shows the highest peak at 16.20 d with SDE=76.2. The dashed blue lines indicate the aliases of this period.

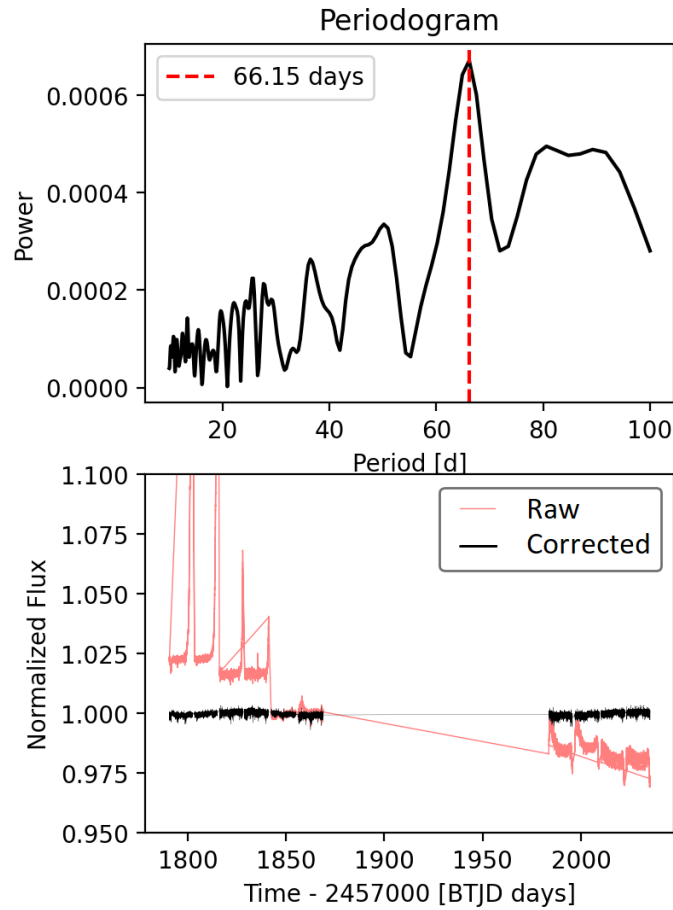


Fig. B.2: Systematics-insensitive periodogram and SAP TESS data for HD207897. *Top*: The SIP periodogram is generated for HD207897. *Bottom*: Raw SAP TESS light curves in red and detrended data against instrument systematics by SIP in black. The SIP periodogram does not exhibit any significant signal for HD207897 b because the highest peak in this periodogram has a power of only 0.0006 at 66.6 d.